MNRAS 000, 1–29 (2022) Preprint 1 July 2022 Compiled using MNRAS LATEX style file v3.0

Non-solar abundance ratios trends of dEs in Fornax Cluster using newly defined high resolution indices

Şeyda Şen[1,2]★, Reynier F. Peletier[1], Alexandre Vazdekis[3,4]

[1] *Kapteyn Astronomical Institute, University of Groningen, P. O. Box 800, 9700 AV Groningen, Netherlands*
[2] *Sabancı University, Faculty of Engineering and Natural Sciences, İstanbul 34956, Turkey*
[3] *Instituto de Astrofísica de Canarias,Calle Vía Láctea s/n, E-38200 La Laguna, Tenerife, Spain*
[4] *Departamento de Astrofísica, Universidad de La Laguna, E-38205 La Laguna, Tenerife, Spain*

arXiv:2206.15214v1 [astro-ph.GA] 30 Jun 2022

Accepted XXX. Received YYY; in original form ZZZ

ABSTRACT

We perform a detailed study of the stellar populations in a sample of massive Fornax dwarf galaxies using a set of newly defined line indices. Using data from the Integral field spectroscopic data, we study abundance ratios of eight dEs with stellar mass ranging from 10^8 to $10^{9.5}$ $M_\odot$ in the Fornax cluster. We present the definitions of a new set of high-resolution Lick-style indices to be used for stellar population studies of unresolved small stellar systems. We identify 23 absorption features and continuum regions, mainly dominated by 12 elements (Na, Ca, Sc, Ti, V, Cr, Mn, Fe, Ni, Y, Ba and Nd) in the wavelength range 4700 - 5400 Å and characterise them as a function of age, metallicity and alpha element abundance ratios. We analyse eight dEs and interpret the line strengths, measured in our new high resolution system of indices, with the aid of stellar population models with high enough spectral resolution. We obtain abundance ratio proxies for a number of elements that have never been studied before for dwarf ellipticals outside the Local Group. These proxies represent relative deviations from predicted index-strengths of base stellar population models built-up following the abundance pattern of The Galaxy. The abundance proxy trend results are compared to abundance ratios from resolved stars in the Local Group, and indices from integrated light of larger early-type galaxies. We find that all our dwarfs show a pattern of abundance ratios consistent with the disk of the Milky Way, indicative of slow formation in comparison to their high mass counterparts.

Key words: galaxies: dwarf elliptical – galaxies: evolution – galaxies: individual(Fornax) - galaxies: abundances ratios – galaxies: stellar populations – techniques: spectroscopic

1 INTRODUCTION

The stellar populations of galaxies provide a fossil record of their formation and evolutionary history. An important tool needed to study galaxy evolution is stellar population synthesis. The stellar content and chemical composition of the unresolved stellar populations of galaxies can be obtained by detailed study of the observed absorption features present in their integrated spectra, using the information in the continuum and the absorption line strengths.

Dwarf elliptical galaxies (dEs) are known to exist in large numbers in galaxy clusters Sandage & Binggeli (1984). They give us the opportunity to study the star formation history and chemical evolution not only of these galaxies, but also of galaxy clusters themselves (e.g., Caldwell et al. 2003). On the other hand they are challenging to study because they are intrinsically faint and their metallicities are generally relatively low, so the lines are more difficult to measure.

dEs's appearance is mostly featureless, except for the bright ones, which have components such as disks, spiral arms, bars, lenses, irregular features (e.g. Jerjen et al. 2000; Barazza et al. 2002; Geha et al. 2003; Graham & Guzmán 2003; De Rijcke et al. 2003; Lisker et al. 2006; Ferrarese et al. 2006; Janz et al. 2012, 2014; Su et al. 2021; Michea et al. 2022). Contrary to giant E/S0 galaxies, their surface brightness profiles follow nearly exponential laws[1] (Caon et al. 1993; Ferrarese et al. 2006; Lisker et al. 2007). Kormendy (1985) suggested that they developed their spheroidal, non-star forming and most likely highly flattened appearance (Lisker et al. 2006, 2007) during a transformation from a late-type galaxy when falling into the cluster. In such a way this environmentally-induced transformation created the morphology-density relation (e.g. Boselli & Gavazzi 2014), which is stronger for dwarfs than for giant galaxies.

Over many years, unresolved stellar populations studies have

★ E-mail: senseydastar@gmail.com

[1] https://unishare.nl/index.php/s/pxtKX534Wgo3Fcew

© 2022 The Authors

been done comparing the observed spectrum with a combination of stellar populations models with a range of metallicity and age, and a limited range of abundance ratios. This allows obtaining the Star Formation History (SFH) (i.e, the distribution of stellar ages), the distribution of metallicities, and the abundances of specific key elements. In practise this is done by fitting the full spectrum to models or by measuring line indices, and fitting them to modelled values. Both methods have their own advantages and disadvantages. When using full spectrum fitting approaches one can measure SFHs (e.g. Cid Fernandes et al. 2005; Koleva et al. 2009), but measuring abundance element ratios is not free from problems as there are uncertainties related to stellar atmospheric calculations. Going through line indices has the benefit that it allows obtaining several independent measurements of the abundance of each element and in this way have more control over the measurements. However, as this latter method is generally applied to low resolution spectral indices, only a few very strong lines and abundances of only a number of elements can be measured, and therefore loses the advantage of having many independent measurements of the same quantity. In here, we wanted to make use of our newly defined set of our high resolution indices.

Using low- and medium resolution spectra, a widely used method is to measure spectrophotometric indices, like Lick (Worthey 1994; Worthey et al. 2014) or Rose (1984) indices and compare them to model predictions. Analysing the spectra of galaxies is tougher than it seems because of the age-metallicity degeneracy. Index–index diagram can be used to break the age-metallicity degeneracy in old stellar populations. An optimised version of this age-sensitive indicator is proposed in Vazdekis (1999, 2001). Jones & Worthey (1995) determined that the $H\gamma_{HR}$-Fe4668 diagram can be used to break the age-metallicity degeneracy in old stellar populations. Worthey & Ottaviani (1997) discuss $H\delta$, a line that has lower sensitivity to metallicity, and $H\beta_o$ is the optimized $H\beta$ index, defined by Cervantes & Vazdekis (2009), that is almost not metallicity dependent and therefore a better age indicator. Later on, researchers have continued using this system, since the velocity broadening in massive galaxies is so large that using a higher resolution system would not represent a significant advantage for those objects. For smaller stellar systems, the signal-to-noise ratios (S/N) in the data were often so low that a lower resolution system of indices was often preferred. However, for the smaller systems of this paper, much more information can be extracted if the higher resolution of the data is used. Here, the broadening by stellar motion is so low, that many more lines are measurable than in giant galaxies. With a system of high resolution indices we get a better handle on the abundance distribution in these systems.

Integrated galaxy spectra contain the imprinted chemical evolution of these objects. For instance, massive elliptical galaxies are enhanced in [Mg/Fe] but lower-mass galaxies are not. More local observations indicate that the relative scarcity of low metallicity stars in the solar vicinity does not match predictions from simple galactic chemical evolution models ('G-dwarfs problem') in The Galaxy (e.g. Searle & Sargent 1972), besides the G-dwarf problem also appears in external galaxies like M31 (Worthey et al. 1996). We know much less about the stellar populations of dwarf elliptical galaxies than about their more massive counterparts, which have been studied on an individual galaxy basis and by using surveys such as SDSS, Manga or SAMI.

The stellar populations of dE's span a wide range of subsolar metallicities, from [M/H] ~ -0.1 to -1.5, and mean ages from 1 to 14 Gyr (Caldwell et al. 2003; Michielsen et al. 2008; Paudel et al. 2010; Koleva et al. 2011; Toloba et al. 2014; Ryś et al. 2015; Sybilska et al. 2017, 2018; Şen et al. 2018). Also, they do not consist of simple, old and metal rich stellar populations, but span a range in ages and are relatively metal poor systems (Michielsen et al. 2008; Koleva et al. 2009; Ryś et al. 2015).

Stellar population studies show that unresolved dEs have on average a lower metal content than giant ellipticals, as expected from the metallicity-luminosity relation (Michielsen et al. 2008; Skillman et al. 1989; Sybilska et al. 2017). Their effective ages are somewhat younger on average, giving evidence of downsizing (Vazdekis et al. 2004; Nelan et al. 2005; Thomas et al. 2005; Sybilska et al. 2017; Caldwell et al. 2003). However, recent studies show that the stellar populations of dEs show indications of both young and old ages and a range in gradients (e.g. Koleva et al. 2009, 2011; den Brok et al. 2011; Ryś et al. 2015; Hamraz et al. 2019), in agreement with the few dEs in the Local Group. However studies about detailed abundance ratios in dEs are scarce. Gorgas et al. (1997); Michielsen et al. (2008); Sybilska et al. (2017) and Şen et al. (2018) show that [Mg/Fe] is around solar, although not without scatter, lower than what is found in giant ellipticals, with [Mg/Fe] possibly going up for decreasing metallicity. Very little is known about the abundance ratios for other elements, mainly because of the lack of high S/N spectra, but also because of the lack of methods and models to properly analyse them. In Şen et al. (2018) abundance ratios of [Ca/Fe] and [Na/Fe] are given for a sample of 39 Virgo dwarf ellipticals. [Ca/Fe] is found to be slightly larger than solar, while [Na/Fe] is considerably lower than solar. This is in sharp contrast with massive ETGs (see, e.g., Vazdekis et al. 1997 for Ca and La Barbera et al. 2017 for Na).

Most spectroscopy of dEs in the literature have been taken using long-slit instruments, and is therefore sensitive to aperture effects, the slit being almost always very narrow. With new Integral Field Spectroscopy this problem disappears, since a large part of a galaxy is covered in the integral-field unit (IFU). It is therefore much easier to produce high integrated S/N spectra than with long-slit spectroscopy, particularly for achieving high spectral resolution, which requires narrowing the slit. Current IFU surveys (e.g. ATLAS 3D , SAMI, MANGA) do not include dEs due to low surface brightness and small size. Notably are the dwarfs observed with MANGA, and with stellar mass between 10^9 and 5.10^9 $M_\odot$ (Penny et al. 2016, 2018) and the IFU observations using SAURON of ~ 10 dEs by (Ryś et al. 2013). A high resolution study of the internal kinematics of dwarf galaxies in the Fornax Cluster, using observations of the SAMI instrument at a resolution of 5000, was recently published by Scott et al. (2020). Also, internal kinematics have been published of an infalling group of galaxies into the Virgo Cluster, by Bidaran et al. (2020), using the MUSE instrument. These studies have revealed that dEs are generally pressure supported stellar systems (Ryś et al. 2014; Toloba et al. 2015; Scott et al. 2020; Bidaran et al. 2020), rotating even slower than their giant counterparts.

This paper is designed as a two-part to understand the stellar populations of dwarf elliptical galaxies (dEs). In a first part we defined a system of high resolution absorption line strength, consisting of 23 indices measuring transitions of 12 elements. We investigated their behavior as a function of age, metallicity and [α/Fe] abundance ratio. Here we aim at studying the processes that formed dEs by analysing their absorption line spectrum in detail. We will not use either classic Lick index or full spectral fitting approaches, but use the fact that dwarf ellipticals show only limited internal broadening, so that a newly defined system of high resolution absorption line indices can be used. In this way we can measure the indices of the system we defined in this paper. At the end of the paper, we will compare our results with other galaxies. These are mainly those in

the Local Group, where individual stars have been observed, and those of giant ellipticals from integrated spectra.

This paper is organised as follows. In Section 2 and 3, we describe the galaxy sample and the spectroscopic data we use in this paper, the instrumental setup used for the spectroscopic observations, and the main steps in the data reduction. In Section 4, we derive the mean luminosity weighted ages and metallicities of our galaxies based on age-sensitive and metallicity-sensitive indices. In Section 5, we introduce the new set of high-resolution line indices that we define and the method used for the definition and we characterise the dependence on age and metallicity of the indices and also investigate the dependence of the line indices on alpha-elemental abundance ratios. In Section 6, we present the measurement of the new set of high-resolution line indices for the dEs. In Section 7, we compare the galaxies with Pegase-HR SSP models, to find out how the abundance ratio proxies compare with the ones in the solar neighborhood. In Section 7, we present the results, ordered by groups of elements and discuss them.

2 SAMPLE AND OBSERVATIONS

Our sample of dE galaxies is a subsample of the dEs observed by Scott et al. (2020) using the SAMI IFU. This sample was selected from the FDS dwarf sample (Venhola et al. 2018). For this paper we selected 8 dwarfs with high S/N spectra, stellar masses between 10^8 $M_\odot$ and $10^{9.2}$ $M_\odot$, and with integrated velocity dispersions between 10 and 40 kms^{-1}. Venhola et al. classify them as dE and their properties (see Table 1) are representative for bright dwarf galaxies. Given that their effective radii range from 5 to 15 arcsec the spectra cover a region up to 0.5-1.5 R_e of the galaxy, appropriate for mapping stellar kinematics and extracting stellar populations representative of the whole galaxy. Three galaxies in our sample, FCC135, FCC182 and FCC203 are classified as disky from unsharp masking (Michea et al. 2022). Unsharp masking makes an effective way to examine if faint substructure features are embedded in the bright diffuse body of a galaxy. In Michea et al. (2022) disk structures show bars, spiral arms, rings and generally have the same colors as the galaxies, while clump substructures enclose irregular light over-densities such as star forming regions, dust lanes and off-center nuclei. None of our sample is classified as clumpy. In Fig. 1 we show the locations of our galaxies in Fornax cluster. They are all located within the Virial Radius, in the center of the cluster.

All observational data were obtained at the Sydney – Australian Astronomical Observatory (AAO) Multi-Object Integral-Field spectrograph (SAMI; Croom et al. 2012) which is mounted at the prime focus of the 3.9m Anglo-Australian Telescope (AAT) at Siding Spring Observatory, New South Wales.

SAMI is based on lightly fused fibre bundles called hexabundless (Bland-Hawthorn et al. 2011; Bryant et al. 2011, 2014). SAMI consists of 13 hexabundles, each having an on-sky diameter of 15″. Besides 13 hexabundles, SAMI also has 26 individual sky fibres which allows us sky subtraction for all IFU observations without the need to observe separate blank sky frames. SAMI can target 13 galaxies in a single observation, or more likely 12 galaxies and one standard calibration star, significantly decreasing the amount of time needed to build a large sample of galaxies with IFS data. This standard star is useful for several important steps in the data reduction (e.g. telluric correction, absolute flux calibration), in addition to allowing us to figure out the point spread function and transmission of each individual observation.

AAOmega is a double-armed spectrograph covering the blue and red optical spectral regions. AAOmega allows variable wavelength coverage and spectral resolution in each arm. Our configuration for SAMI uses the 1500V grating in the blue arm, giving R= $\lambda/\Delta\lambda \sim 5000$ over the wavelength range 4660-5430 Å.

For this work we are primarily interested in fitting the stellar absorption features covered by the blue arm of AAOmega, and therefore we analyse only this arm. This spectral range has been widely used for detailed stellar populations studies. In this work we are pushing forward its potential by performing the analysis at higher resolution.

The observing strategy is taken from the SAMI Galaxy Survey (Sharp et al. 2015). The galaxies were observed on 4^{th} – 8^{th} Nov 2015 and 26^{th} – 30^{th} Oct 2016. For each field we aimed to obtain 7 hours ($\sim 25,000$ seconds) of on-source integration time. Individual integrations were $\sim$ 1800 s, with dithers of 0.″8 (half a fibre diameter) applied between exposures, following a 7-point hexagonal dither pattern, optimised for the SAMI hexabundles. The dither pattern ensures an even distribution of S/N over a hexabundle, accounting for the gaps between fibres. This 7-point dither pattern was repeated twice for each field, yielding $\simeq 25,000$ second total exposure time per galaxy. Arc lamp calibrations and observations of primary spectophotometric standard stars from the European Southern Observatory Optical and UV Spectrophometric Standard Stars catalogue[2] were interspersed with the object exposures at regular intervals.

The dEs galaxies were observed with SAMI using the 1500V grating in the blue arm. This grating provides a spectral resolution that is sufficient to resolve the typical velocity dispersion of dwarf galaxies of 20-30 km s^{-1}. In addition, it also covers the principal stellar absorption features (e.g. $H\beta$, Fe5015, Mgb) and the newly defined high-resolution line indices of Section 5, which were designed to measure relevant stellar population properties. Figure 2 shows the normalized spectra of our sample dEs taken with the SAMI, identified by their names.

3 DATA REDUCTION

The reduction of the SAMI observations is described in Scott et al. (2018), with further details provided in Sharp et al. (2015) and Green et al. (2018). Our SAMI data were reduced using the *sami* Python package (Allen et al. 2015). Here we briefly summarise the process and give in detail the changes with respect to the previous works.

The SAMI data reduction was performed in two main steps; the first takes the data from raw observed frames to Row-Stacked Spectra (RSS) frames, which is handled primarily to partially calibrated spectra from each fibre of the instrument, including spectral extraction, the standard steps of bias subtraction, flat-fielding, wavelength calibration and sky subtraction by the two-degree field data reduction software package (2dfDR[3]). The second step takes the data from RSS frames to flux-calibrated, three-dimensional data cubes, utilising purpose-built Python software as part of the *sami* package. The entire process is overseen by the *sami* Python *manager*.

Moreover, spectra corresponding to individual fibres are extracted using 'tramlines' fits to observations of the twilight sky. Subsequent to the fibre extraction, telluric correction and relative

[2] Available at:
https://www.eso.org/sci/observing/tools/standards/spectra.html
[3] https://www.aao.gov.au/science/software/2dfdr

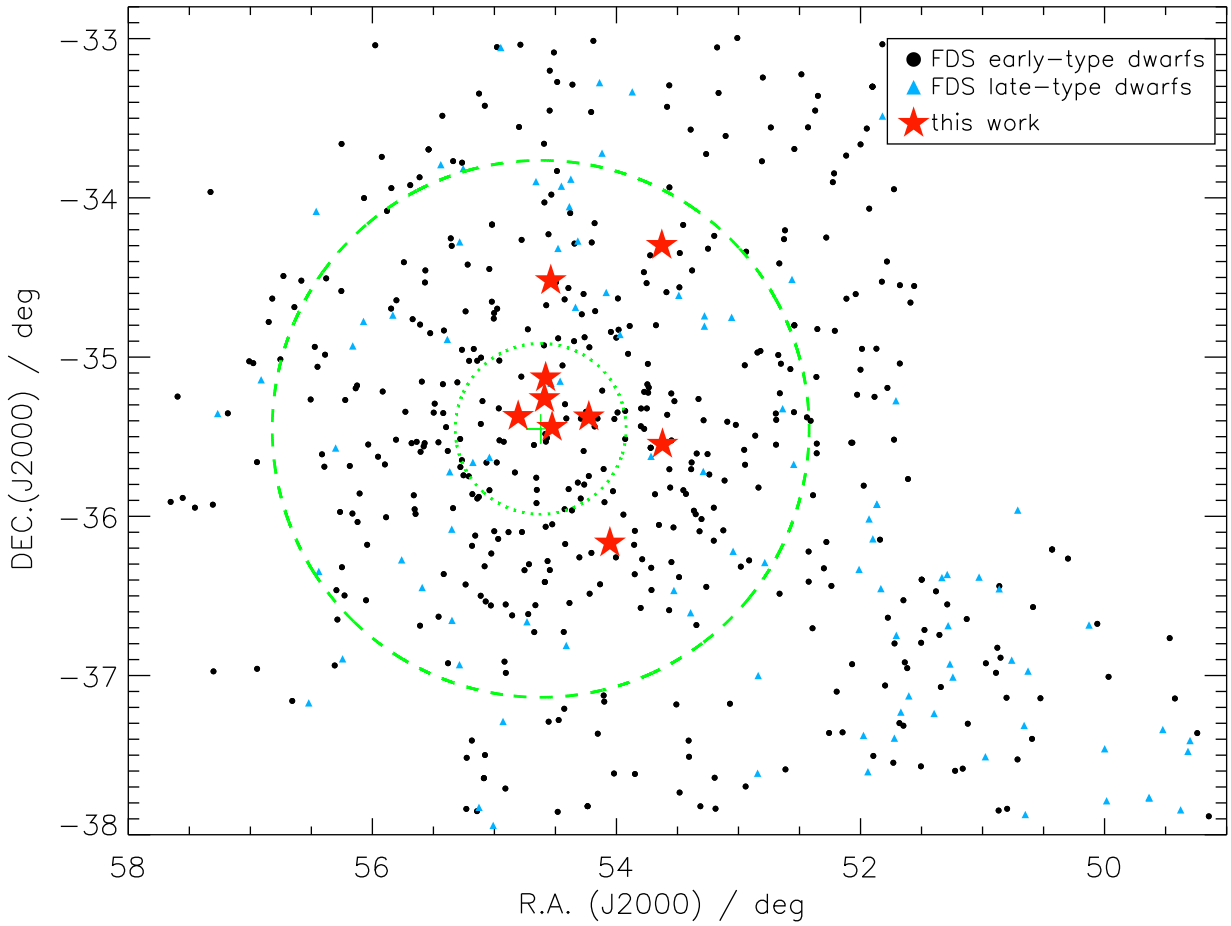

Figure 1. Map of the Fornax cluster. The black and blue symbols correspond to early-type dwarfs and late-type dwarfs from Venhola et al. (2018), respectively. The red stars represent our sample. The green dotted circle and lashed circle shows the core (Ferguson 1989) and the virial radius of 2.2deg (~ 0.7 Mpc, Drinkwater et al. 2001) respectively. The green cross shows the central galaxy NGC 1399.

Table 1. Properties of the dEs in Fornax Cluster . Column 1: galaxy name. Columns 2: FDSDC name by Venhola et al. (2018). Columns 3 and 4: right ascension and declination in J 2000. Columns 5 and 6: r-band and g-band magnitude (in the AB system), Columns 7: half-light radius by Venhola et al. (2018). Column 8: velocity dispersion from Eftekhari et al. (in preparation). Column 9 and 10: ellipticity and morphological classes from Venhola et al. (2018); e = smooth early-type, e* = smooth early-type, object has a nucleus, e(s) = early-types with structure, e(s)* = early-types with structure, object has a nucleus Column 11: stellar mass. Column 12: date observed.

Galaxy	FDS	RA (deg)	Dec (deg)	M_r (mag)	M_g (mag)	R_e (arcsec)	σ_e (kms^{-1})	ϵ	Morph. Class	log ($M \star / M_\odot$)	Date observed
FCC135	F15D384	53.628	-34.297	-16.8	-16.2	14.7	21.2 ±2.8	0.53	e(s)	8.708 ±0.003	Oct 2016
FCC136	F16D159	53.623	-35.546	-17.8	-17.0	17.5	30.9 ±1.6	0.13	e	9.082 ±0.003	Oct 2016
FCC164	F12D367	54.054	-36.166	-16.0	-15.4	10.0	11.1 ±5.2	0.45	e(s)	8.335 ±0.003	Oct 2016
FCC182	F11D279	54.226	-35.375	-17.9	-17.1	9.7	38.9 ±0.5	0.04	e(s)*	9.168 ±0.002	Oct 2016
FCC202	F11D235	54.527	-35.440	-17.3	-16.6	13.3	31.5 ±1.0	0.41	e*	8.909 ±0.003	Nov 2015
FCC203	F10D189	54.538	-34.519	-16.9	-16.3	16.0	31.4 ±2.3	0.45	e(s)	8.757 ±0.003	Oct 2016
FCC211	F11D339	54.590	-35.260	-16.1	-15.5	6.6	20.1 ±5.7	0.25	e*	8.339 ±0.003	Nov 2015
FCC222	F11D283	54.806	-35.371	-17.0	-16.3	16.1	18.6 ±3.8	0.11	e*	8.771 ±0.003	Nov 2015

and absolute flux calibration steps are performed utilising the spectrophometric standard star and standard calibration star observations. Finally, the data for each individual object are extracted from the RSS frames and combined into a three-dimensional data cube using a drizzle-based algorithm.

At the end, we add the spectra of the whole SAMI-field to get an integrated spectrum. More details on observations and data reduction are presented in Scott et al. (2020) (S20).

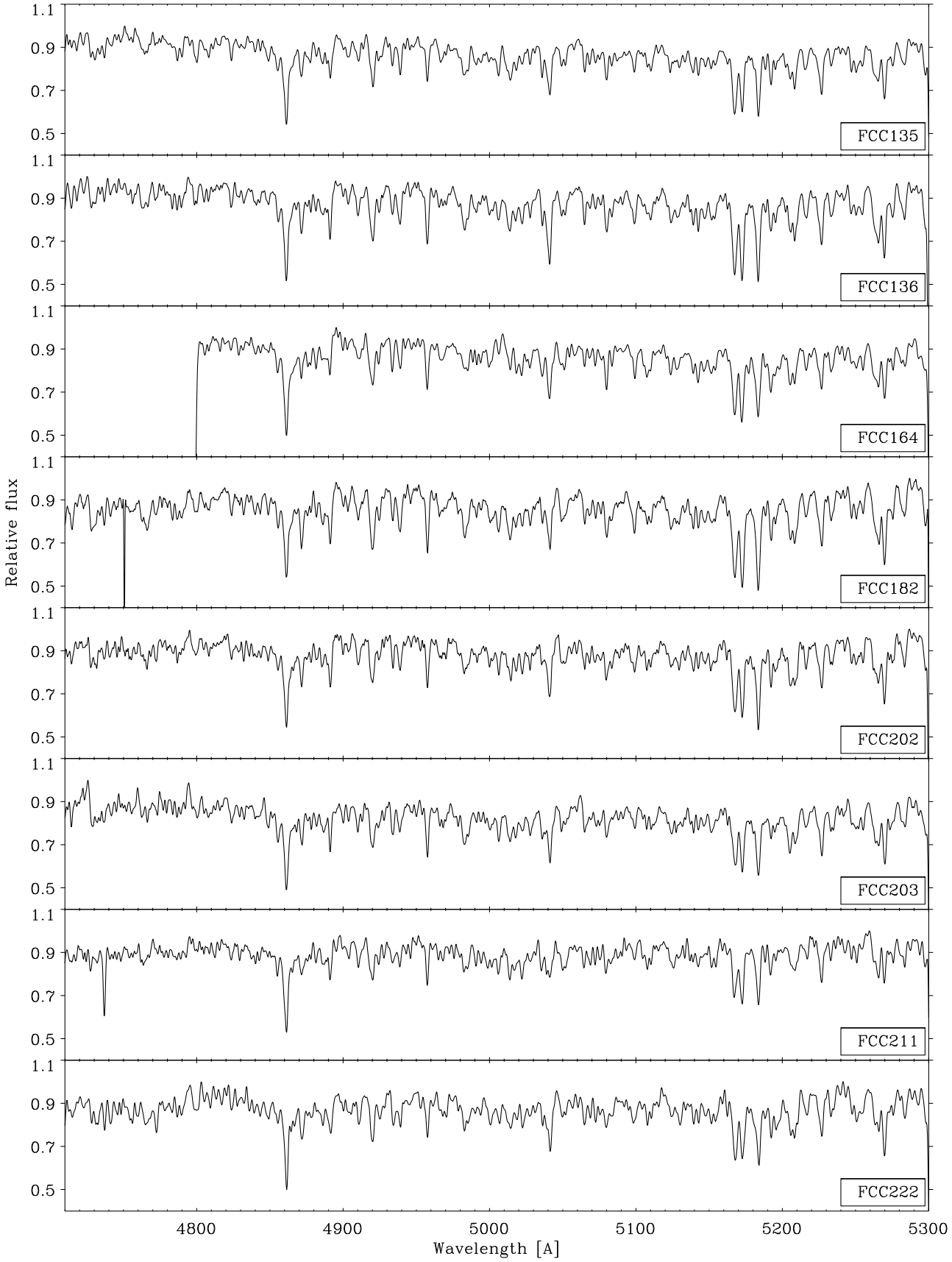

Figure 2. Normalized spectra of our 8 dEs taken with the SAMI.

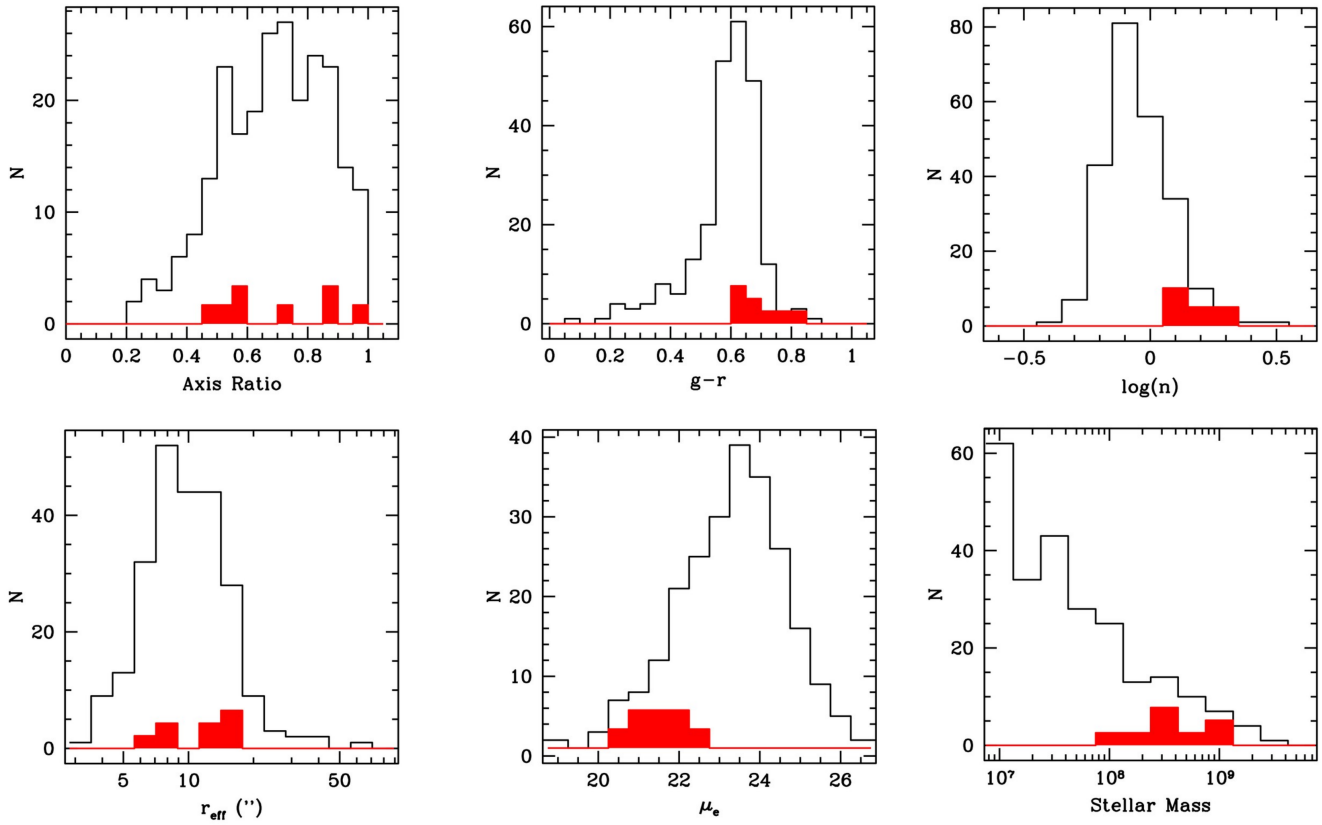

Figure 3. Properties of our sample, as compared to the sample of all dwarf galaxies more massive than 10^7 $M_\odot$ of the Fornax Cluster (Venhola et al. 2019, in black). The galaxies considered in this paper are plotted in filled red.

4 AGE AND METALLICITY DERIVED USING STANDARD INDICATORS

In this paper the process of determining abundance ratio proxies of various elements goes as follows. We first determine a mean luminosity weighted age and metallicity using standard age- and total metallicity-sensitive indicators ($H\beta_o$ and [MgFe50]). After that we use a set of high resolution absorption line indices (see Section 5.1) to compare our galaxies with SSP model predicted indices for the derived age and metallicity. This gives an uncalibrated comparison, showing whether the index values for a certain galaxy are lower or higher than expected. These values are tabulated in Table A3. Given that models to calibrate such relative deviations are not available at the required resolution, we decided to only give these proxies, which themselves are very instructive and tell us about the way these galaxies were assembled. In this section we give details on how the ages and metallicities were calculated. In the next section the indices are defined.

To obtain the mean luminosity-weighted age and metallicity we assume that the galaxies are fitted with single-age and single-metallicity SSP models. This is done by measuring the age-sensitive ($H\beta_o$) and metallicity-sensitive (Fe5015 and Mg b) Lick spectral indices (Worthey 1994). Before measuring the indices we broadened our data out to σ = 40 km s^{-1} to match the PEGASE.HR (Le Borgne et al. 2004) SSP models then calculated the index values. We minimize the possible influence of abundance ratios on the derived SSP metallicity by using the abundance-ratio insensitive index combination [MgFe50] (Kuntschner et al. 2010) and the $H\beta_o$ index (Cervantes & Vazdekis 2009), which is less dependent on metallicity than the standard Lick $H\beta$ index.

We use the grids of PEGASE.HR SSP models (with ages from 1 to 14 Gyr and [Fe/H] from -1.7 to 0.4) to match the data with stellar population models. Then, we obtain best-fit population parameters by effectively computing the "distance" from our measured indices to all the predicted values of those indices on the finer grid, and finding the age-metallicity combination with the minimum total distance. We estimate the ages and metallicities ([M/H]) using the software RMODEL (Cardiel et al. 2003). This software interpolates the age and metallicity inside an index-index grid. The errors in the age and [M/H] are calculated by running 1000 Monte Carlo simulations, varying the values of the spectral indices within a Gaussian function whose width is equal to their uncertainties.

Fig. 4 shows $H\beta_o$ as a function of the [MgFe50] index plots where we have restricted the age to the interval 3.5 - 14.0 Gyr, and the metallicity range from -1.70 to 0.00, which cover the range of solutions of our galaxies. Both luminosity weighted age and metallicity were computed, which are given in Table 2. We then compared with the MILES models (Vazdekis et al. 2010) after smoothing the data σ = 60 km s^{-1} , i.e. the nominal resolution of these models. The results are shown in Fig. 5. We find a good agreement between the results obtained with these two models, although a small shift of about 0.1 dex is found for the derived metallicities and about 1.0 Gyr for the mean ages.

We find that while the metallicity of these galaxies vary between [Fe/H]~ -0.2 to ~ -0.9, while show a mean age ~7.0 Gyr. This explains why we can use an approach based on a single SSP.

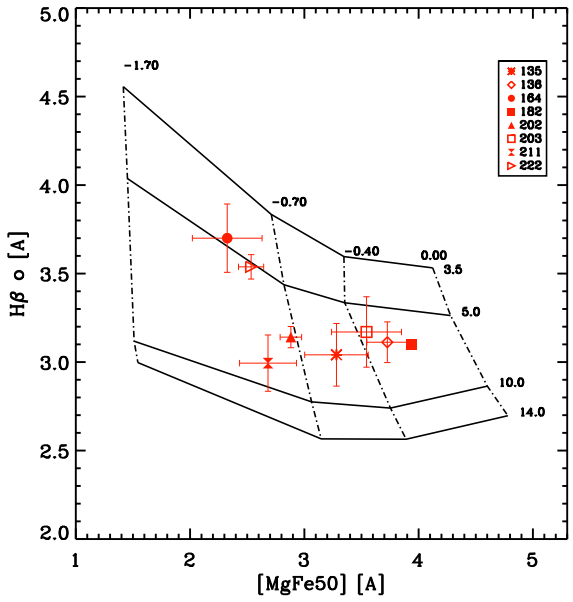

Figure 4. $H\beta_o$ vs. [MgFe50] line-strength, overplotted on the grid of PEGASE.HR (Le Borgne et al. 2004) SSP models predictions with σ = 40 km s^{-1}. Solid lines indicate constant age 3.5, 5.0, 10.0 and 14.0 Gyr, respectively, while dotted lines indicate constant [M/H] -1.70, -0.70, -0.40 and +0.00, respectively.

Note that if the mean luminosity-weighted ages were not as old we would require considering younger components on the top of the dominating old population to be able to properly fit the data.

Studies have shown that lower-luminosity early-type galaxies show a wider range in age than their more luminous counterparts (e.g. Worthey & Ottaviani 1997; Kuntschner & Davies 1998; Caldwell et al. 2003) Some studies find that the star formation histories of early-type galaxies depend on cluster properties and environment (Sánchez-Blázquez et al. 2003; Trager et al. 2000). The Fornax cluster is more compact than the larger Virgo cluster, making it a good target for the study of environmental influences and obtaining a better picture of galaxy formation (Jordán et al. 2007).

Kuntschner (2000) concluded that all their ellipticals in Fornax cluster show a uniformly old age, forming a sequence in metallicity varying roughly from -0.25 to 0.30 in [Fe/H]. Furthermore, the S0 galaxies in his sample, which, at the same time, were usually of lower mass, generally had lower ages (Kuntschner & Davies 1998).

5 A HIGH RESOLUTION LINE INDEX SYSTEM

Here we present the definition of a new set of high-resolution Lick-type spectral indices, which make it possible to give a proxy on the abundance ratios in systems with low stellar velocity dispersion, such as dwarf galaxies, globular clusters, UDGs etc. Although some high-quality, high-resolution spectroscopic data for dEs is available, the problem is that current spectral indices are defined for low resolution spectra, which is not optimal for studying the fainter lines. To achieve this, we have used the ELODIE high resolution spectra (Prugniel & Soubiran 2001, 2004) to define a set of new indices covering transitions involving as many elements as possible. Indices should depend as little as possible on spectral resolution,

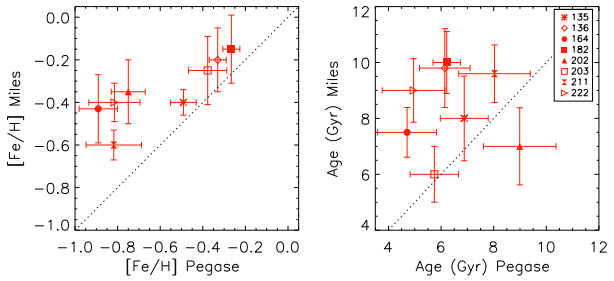

Figure 5. Comparison between PEGASE.HR and MILES models with σ = 60 km s^{-1}.

and, ideally, be located in isolated patches of the spectrum with minimal crowding.

The ELODIE library is a stellar database of 1959 spectra for 1503 stars, observed with the echelle spectrograph ELODIE on the 193 cm telescope at the Observatoire de Haute Provence. The typical signal-to-noise (S/N) ratio of the spectra is 500 Å^{-1}. It has a large coverage of atmospheric parameters : $T_{\rm eff}$ from 3000 K to 60000 K, log g from -0.3 to 5.9 and [Fe/H] from -3.2 to +1.4. The library provides spectra at two different resolutions (R=42000 and R=10000), where we used R=10000 calibrated in physical flux (σ = 12.7 km s^{-1} at FWHM = 0.55 Å).

We use a grid of single age and single metallicity (SSP) stellar population models computed with the evolutionary synthesis code: PEGASE.HR (Le Borgne et al. 2004). These models are based on the empirical stellar library ELODIE.3 (Prugniel & Soubiran 2001, 2004). The SSP models have a range of -1.7 to 0.4 in metallicity [Fe/H] and 1 Myr to 20 Gyr in age. As the ELODIE stars follow the abundance pattern of the Milky-Way the resulting PEGASE.HR (Le Borgne et al. 2004) models also follow this pattern.

5.1 Index Definitions

Since the galaxy spectra that we analyse in this paper cover the range $\lambda\lambda$ 4700-5400 Å, we identified major absorption features and continuum regions in this spectral range using the spectral atlas of Arcturus[4]. Once selected, for each line we pre-defined three wavelength bands containing the feature and two pseudocontinua on both the blue and red sides of the central feature. The line indices are determined using their pseudo-equivalent width, which one gets by integrating the ratio between the pseudocontinuum and the flux over the central or index passband.

The lines are chosen from the Atlas of Arcturus to study as many elements as possible by defining indices around features which contain absorption lines from transitions of these elements, selecting lines that are as isolated as possible, together with continuum bands as devoid of lines as possible.

The initial definition provided us with a first look into the general behaviour of the index as a function of age, metallicity and velocity dispersion (σ). After analysing this pre-definition, we improved it for each index. This is done by means of an automatic program that performs a multidimensional maximisation of index values. This programme changes the limits of the central feature and the two pseudocontinuum bands, around their initial values

[4] http://spectra.freeshell.org/spectroweb.html

and for each new definition, it measures the value of the index for the whole set of models and finds the maximum value of the index. When doing this we made sure that the feature and continuum bands did not shift by more than 5 Å from the original guess. After that we checked each lines by eye to make sure not including another absorption from a different element.

We measured the newly defined indices for the whole grid of models (with ages from 0.1 to 13 Gyr and metallicities from -1.7 to 0.4 [Fe/H]), at a velocity dispersion of $\sigma \sim 25$ km s^{-1}, which is typical for these objects (Eftekhari et al., submitted to MNRAS). We also study the effect of changing the resolution by broadening the spectra with velocity dispersions out to $\sigma = 130$ km s^{-1}. Figure B1 shows the results for some indices, where we have plotted index versus [Fe/H] and age, respectively and their dependence on σ. All the other indices are shown in Figure B2- B4 in the Apendix B. In general all the index value decrease with increasing sigma but some being more stable than the others. Among the most stable indices in the covered velocity resolution range are Fe4920, Cr5265, Sc5083 and V4924.

We also measured the indices of Elodie stars with $\sigma = 25$ km s^{-1} (which corresponds to R=5000) to understand better the dependence on age and metalicity. All of line indices are shown in Figure C1- C4 in the Appendix. In Figure C1 we show how the line strength indices change as a function of effective temperature, surface gravity, and metallicity. Remarkably there are a number of indices that are gravity sensitive like Cr4789, Cr5247 and V4924, all achieving larger index values for giant stars. We will investigate their potential to constrain the IMF in low velocity dispersion systems in a forthcoming paper.

We list the features that we defined in Table A1. The index name is composed of the element or elements that the index targets, along with the central wavelength of the index passband. Wavelengths are listed in units of angstroms. None of the features in Serven et al. is included, since they are meant for low resolution spectra. From the original Lick system we only include the Mg *b* index, since this is the only strong Mg-line in this part of the spectrum.

We tried to obtain at least one or more indices per element for as many elements as possible, with equivalent widths larger than 0.2 Å in order to be able to measure the index well. For Fe and Ti there were so many lines that we only selected some of the brightest features. We also tried to select indices that were mostly dependent on age or metallicity, although most indices are dependent on both (Section 5.3).

5.2 Age and Metallicity Indicators

In this section we characterise the dependence on age and metallicity of the indices. To do this, we calculate partial derivatives of the indices with regards to age and metallicity. For this we consider the indices i for 25 representative SSP-models of different ages ($j = 1, ..., N_j = 5$) (t=0.1, 0.3, 1, 3, 13 Gyr) and metallicities ($k = 1, ..., N_k = 5$) ([Fe/H]= -1.7, -0.7, -0.4, 0.0, 0.4), and estimate the slope of the iso-metal lines, β, and of the isochrones, α, in those points. For each point equation (1) and equation (2) give the definitions for α_i and β_i, respectively, where I is the index name, Z is the metallicity [Fe/H], and t represents the age.

$$\alpha_i(t_j) = \left| \frac{\delta I_i(Z,t)}{\delta Z} \right|_{t_j} \qquad (j = 1, ..., N_j) \qquad (1)$$

$$\beta_i(Z_k) = \left| \frac{\delta I_i(Z,t)}{\delta \log t} \right|_{Z_k} \qquad (k = 1, ..., N_k) \qquad (2)$$

We now get the average, relative dependence of the index i on metallicity by averaging the N_j (in this case 5) ages:

$$A_i = \sqrt{\frac{\sum_{j=1}^{N_j} \left(\frac{\alpha_i(t_j)}{I_i} \right)^2}{N_j}} \qquad (3)$$

and the dependence of the index i on age is given by Equation 4.

$$B_i = \sqrt{\frac{\sum_{k=1}^{N_k} \left(\frac{\beta_i(Z_k)}{I_i} \right)^2}{N_k}} \qquad (4)$$

Figure D1 shows the values of A_i and B_i for each index i grouped per element. Data points near the X-axis are metallicity-indicators, while the ones near the Y-axis are age indicators. We list the values of A_i and B_i for each index i Table A2. Most of our line indices are affected by metallicity and age. We indicate some indices that are more sensitive to age or metallicitiy as listed in Table A2.

5.3 Dependence on [α/Fe]

The chemical abundance patterns in the spectra of stellar population are a direct tracer of histories of star formation and chemical enrichment of galaxies. So, in order to be able to measure not only metallicity but also abundance ratios of alpha elements we investigated the dependence of the line indices on alpha-elemental abundance ratios using the theoretical models of Walcher et al. (2009) (hereafter W09). The SSP-spectra in the age range 2-13 Gyr, for abundance values [Fe/H] = -0.5 to 0.2 and [α/Fe] = 0.0 and 0.4 at a constant resolution of FWHM = 1 Å. This leaves us with powerful models to study high/medium resolution galaxy spectra. Note that these are fully theoretical models, i.e. based on the Coelho et al. (2005) library of theoretical stars.

We compare the models of two different α-element-to-iron abundance ratios ([α/Fe] = 0.0 and 0.4) for the newly defined indices. When enhancing the abundances of the α-elements, the abundances of the Fe-peak elements are decreased in order to keep the total metallicity fixed. Here we measure abundances of the α-elements Mg, Ca and Ti (see Figure 6) and the Light odd-Z element: Na (see Figure 7) in addition to the Fe–peak elements Cr, Mn, Fe, Co, Ni, Sc and V (see Figure 8).

Indices characterised to be insensitive to α/Fe can be defined as a good age or total metallicity indicators. Figures 6 and 8 show that for the alpha enhanced models the α-elements are seen to increase in strength, as expected, while the Fe-peak elements have similar strengths as for the models at solar abundance ratio, or are slightly weaker. The heavy elements shown in (Fig. 9 behave in the same way as the Fe-peak elements.

6 GALAXY MEASUREMENTS

Unlike for massive galaxies, high resolution spectroscopy can provide accurate measurements of numerous absorption lines for many different chemical elements in dwarf galaxies, making it easier to derive their abundance pattern. Line indices are an effective way of analysing results as one can reduce the spectral data to simply

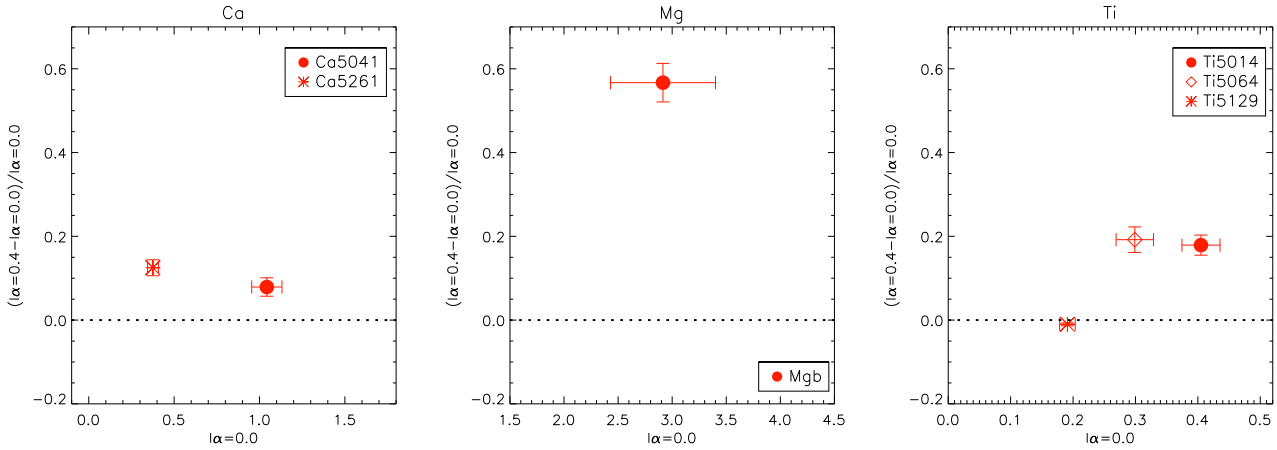

Figure 6. Differences between the alpha-enhanced predictions ([α/Fe] = 0.4) and the solar-scaled ones ([α/Fe] = 0.0) for α-elements. On the x-axis is given the index at solar α/Fe.

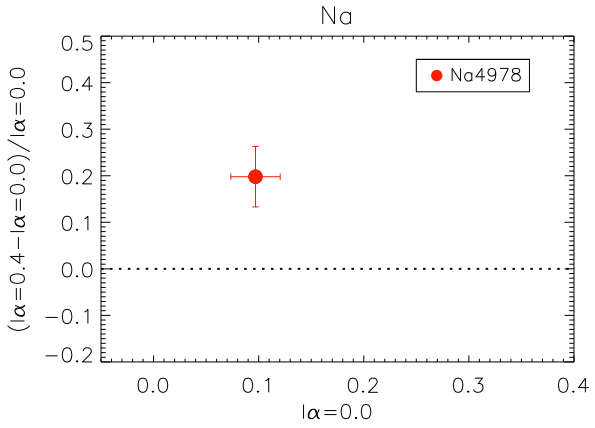

Figure 7. Differences between the alpha-enhanced predictions ([α/Fe] = 0.4) and the solar-scaled ones ([α/Fe] = 0.0) for the light odd-Z element: Na. On the x-axis is given the index at solar α/Fe.

a single number plus its error. In this work we study a new set of high-resolution spectral indices (Section 5.1), analogous to the Lick system in that the indices are defined by means of a blue and a red bandpass at either side of the feature bandpass. The given name corresponds to the element that the index targets, along with the central wavelength of the feature bandpass.

SAMI utilised the 1500V grating in the blue arm, giving R~5000 over the wavelength range 4660-5430 Å. The indices were calculated using the package REDUCEME (Cardiel 1999). For the interpretation of these high-resolution indices we focus on 23 indices which show good correlation with mass to study the abundance measurements.

For our galaxies the index measurements with errors in angstroms of equivalent width which we used in this work are given in Table 2.

6.1 Comparison of data with stellar population models

We use the single age and metallicity (SSP) stellar population models computed with the evolutionary synthesis code: PEGASE.HR (Le Borgne et al. 2004). These models are based on the empirical stellar library ELODIE.3 (Prugniel & Soubiran 2001, 2004) which has a range of -1.7 to 0.4 in metallicity [Fe/H] and 1 Myr to 20 Gyr in age.

We convolved all galaxies and all models to the same resolution: the PEGASE.HR models were convolved to an instrumental resolution of σ= 25 kms^{-1}(which corresponds to R=5000, and is the same as the SAMI-resolution), after which all models and all galaxies were convolved to an instrumental velocity dispersion of σ= 40 kms^{-1}. This way all galaxies could be compared at once with each other.

To test what is the effect of the SSP approach for determining age and metallicity on the line strength measurements, we have done some simulations. For each galaxy we determined two solutions: an SSP-solution (with the PEGASE.HR models) best fiting the observed $H\beta_o$ and Mg b of the galaxy, and a model consisting of a linear combinations of SSPs of Z=0.0004 and 15.9 Gyr (PEGASE.HR scale), Z=0.008 and 1 Gyr and Z=0.008 and 8 Gyr, optimally fitting these 2 absorption lines. Comparing the high resolution indices between these 2 solutions then tells us to what extent the one-SSP approximation is affecting our results. The average differences and standard deviations are given in table 3. The differences are around 10%. For some lines slightly more, others slightly less. One gets this difference, because of the influence of the young populations, which make the continuum stronger, and therefore all metal lines weaker. Since the results in this paper are qualitative, this simulation shows that our conclusions will not change.

7 RESULTS

In this work we study the abundance ratios of a sample of 8 bright dwarf elliptical galaxies using a new set of 23 high-resolution spectral indices. We are interested in studying the differences in the abundance ratios with respect to their more massive galaxy counterparts from a qualitative point of view. However, to increase the reliability of our results, we have selected more than 1 index per element, if possible, to have independent measurements to determine the relative abundance of these elements.

The so-called alpha elements, e.g., O, Mg, Ca, Si and Ti, are predominantly synthesised by alpha capture during the various burning phases in massive stars, and expelled into the ISM by SN II

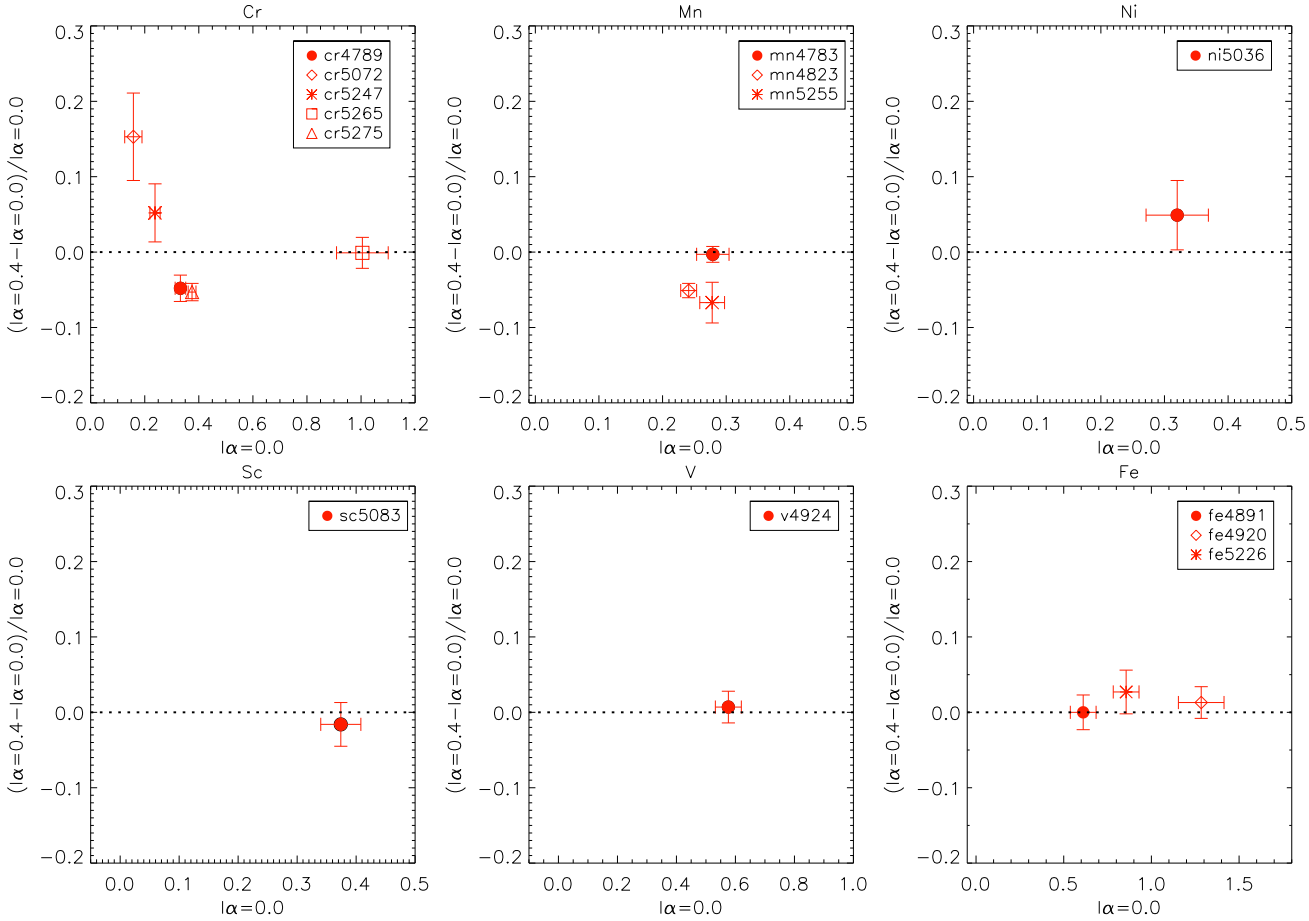

Figure 8. Differences between the alpha-enhanced predictions ([α/Fe] = 0.4) and the solar-scaled ones ([α/Fe] = 0.0) for Fe-peak elements.

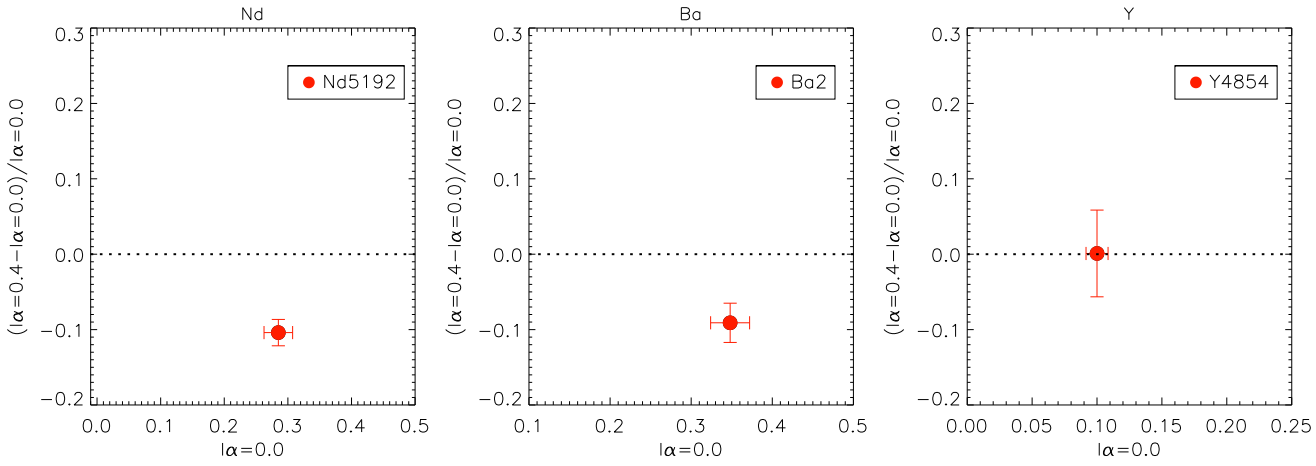

Figure 9. Differences between the alpha-enhanced predictions ([α/Fe] = 0.4) and the solar-scaled ones ([α/Fe] = 0.0) for heavy elements.

explosions. The abundances of the α-elements increase very quickly with time, due to the relatively short main-sequence lifetimes of massive stars. Another group of elements are the Fe-peak elements (Ni, Co, Fe, Mn, etc.) which are mainly produced by SN Ia, whose progenitor lifetimes are much longer. As the evolution of chemical abundances in a given system is closely related to the history of its star formation, abundance ratios such as [α/Fe] can be used to explore the SFH for galaxies.

Heavier elements beyond the iron peak, such as Y, Ba and Nd are synthesized by neutron capture where the two important processes occur (the s- and r- processes), followed by β decays. These two processes lead to two characteristic abundance patterns.

For the interpretation of the spectra, we will start discussing the ages and metallicities of the galaxies. We then focus on the relative abundance pattern as derived from the comparison of the observed indices with PEGASE.HR models at higher resolution. We finish

Table 2. High-resolution spectral indices (as defined in this paper), age and metallicity, measured for 8 dEs in Fornax cluster

	FCC135	FCC136	FCC164	FCC182	FCC202	FCC203	FCC211	FCC222
log age (Gyr)	0.84 ±0.03	0.79 ±0.03	0.67 ±0.04	0.79 ±0.02	0.95 ±0.07	0.76 ±0.03	0.90 ±0.05	0.70 ±0.06
[Fe/H]	-0.49 ±0.06	-0.33 ±0.04	-0.89 ±0.09	-0.27 ±0.04	-0.75 ±0.08	-0.38 ±0.09	-0.82 ±0.13	-0.81 ±0.12
Indices								
Ba2	0.361 ±0.056	0.409 ±0.036	0.333 ±0.060	0.401 ±0.016	0.274 ±0.019	0.219 ±0.066	0.320 ±0.051	0.355 ±0.022
Ca5041	0.991 ±0.074	1.454 ±0.045	0.786 ±0.083	0.944 ±0.021	0.945 ±0.025	1.108 ±0.081	0.742 ±0.065	1.015 ±0.028
Ca5261	0.275 ±0.042	0.387 ±0.026	0.368 ±0.043	0.359 ±0.011	0.314 ±0.013	0.327 ±0.043	0.253 ±0.035	0.215 ±0.015
Cr4789	0.229 ±0.049	0.353 ±0.030	. . .	0.378 ±0.014	0.261 ±0.016	0.338 ±0.050	0.245 ±0.043	0.314 ±0.018
Cr5072	0.134 ±0.030	0.159 ±0.019	0.115 ±0.032	0.191 ±0.008	0.158 ±0.010	0.177 ±0.033	0.130 ±0.027	0.180 ±0.012
Cr5247	0.231 ±0.041	0.245 ±0.027	0.175 ±0.044	0.262 ±0.011	0.214 ±0.013	0.125 ±0.044	0.194 ±0.035	0.194 ±0.015
Cr5265	0.605 ±0.048	1.001 ±0.028	0.692 ±0.050	1.035 ±0.012	0.813 ±0.014	0.800 ±0.047	0.620 ±0.040	0.677 ±0.017
Cr5275	0.268 ±0.048	0.406 ±0.030	0.246 ±0.051	0.404 ±0.013	0.342 ±0.015	0.331 ±0.049	0.258 ±0.041	0.292 ±0.017
Fe4891	0.504 ±0.047	0.612 ±0.030	0.472 ±0.049	0.708 ±0.013	0.617 ±0.016	0.393 ±0.056	0.330 ±0.045	0.515 ±0.019
Fe4920	0.944 ±0.083	1.257 ±0.052	1.116 ±0.086	1.389 ±0.022	0.968 ±0.028	0.778 ±0.097	0.711 ±0.077	0.928 ±0.032
Fe5226	0.812 ±0.093	0.898 ±0.059	0.767 ±0.100	0.931 ±0.025	0.771 ±0.029	0.865 ±0.099	0.520 ±0.081	0.831 ±0.033
Mg *b*	2.288±0.272	2.822±0.173	2.213±0.294	3.367±0.037	2.495±0.087	2.097±0.297	1.984±0.228	1.858±0.102
Mn4783	0.152 ±0.049	0.324 ±0.030	. . .	0.269 ±0.014	0.173 ±0.017	0.221 ±0.051	0.233 ±0.042	0.140 ±0.019
Mn4823	0.183 ±0.039	0.196 ±0.025	0.004 ±0.044	0.237 ±0.011	0.183 ±0.013	0.239 ±0.042	0.146 ±0.035	0.104 ±0.015
Mn5255	0.214 ±0.047	0.309 ±0.029	0.266 ±0.048	0.292 ±0.012	0.260 ±0.015	0.288 ±0.048	0.153 ±0.039	0.300 ±0.017
Na4978	0.102 ±0.043	0.120 ±0.028	-0.002 ±0.048	0.132 ±0.012	0.013 ±0.015	0.071 ±0.050	0.075 ±0.038	-0.058 ±0.018
Nd5192	0.273 ±0.031	0.297 ±0.020	0.340 ±0.034	0.351 ±0.008	0.300 ±0.010	0.180 ±0.034	0.229 ±0.027	0.279 ±0.012
Ni5036	0.350 ±0.048	0.429 ±0.030	0.261 ±0.054	0.456 ±0.014	0.279 ±0.017	0.400 ±0.053	0.301 ±0.042	0.265 ±0.019
Sc5083	0.184 ±0.041	0.350 ±0.025	0.177 ±0.043	0.403 ±0.011	0.328 ±0.013	0.235 ±0.044	0.259 ±0.035	0.223 ±0.016
Ti5014	0.379 ±0.043	0.460 ±0.027	0.270 ±0.044	0.441 ±0.012	0.374 ±0.014	0.388 ±0.047	0.331 ±0.041	0.318 ±0.017
Ti5064	0.264 ±0.044	0.375 ±0.027	0.090 ±0.049	0.312 ±0.012	0.250 ±0.015	0.331 ±0.048	0.229 ±0.039	0.295 ±0.017
Ti5129	0.124 ±0.036	0.181 ±0.023	0.112 ±0.038	0.203 ±0.010	0.210 ±0.012	0.128 ±0.039	0.110 ±0.030	0.169 ±0.013
V4924	0.481 ±0.054	0.526 ±0.034	0.421 ±0.058	0.605 ±0.015	0.384 ±0.019	0.333 ±0.063	0.306 ±0.049	0.469 ±0.021
Y4854	0.128 ±0.041	0.076 ±0.027	0.127 ±0.045	0.143 ±0.012	0.101 ±0.014	0.196 ±0.045	0.137 ±0.037	0.109 ±0.016
Hβ_o	3.041±0.177	3.112±0.115	3.700±0.193	3.101±0.026	3.141±0.060	3.170±0.199	2.994±0.159	3.538±0.069
Fe5015	4.983±0.524	5.505±0.337	3.123±0.575	5.545±0.074	4.042±0.178	5.641±0.577	3.996±0.472	3.785±0.208

Table 3. High-resolution spectral indices: average difference and standard deviation between SSP fit and 3 population fit

Index	average(Δ(3pop - SSP)/SSP)	σ((Δ(3pop - SSP)/SSP))	Index	average(Δ(3pop - SSP)/SSP)	σ((Δ(3pop - SSP)/SSP))
Ba2	-0.169	0.074	Mn5255	-0.112	0.096
Ca5041	-0.103	0.07	Ni5036	-0.117	0.071
Ca5261	-0.06	0.067	Sc5083	-0.069	0.075
Na4978	-0.145	0.131	V4924	-0.049	0.09
Ti5014	-0.109	0.055	Y4854	-0.165	0.133
Ti5064	-0.141	0.069	Nd5192	-0.065	0.059
Ti5129	-0.042	0.073	Fe4891	-0.029	0.08
Cr4789	-0.102	0.09	Fe4920	-0.035	0.087
Cr5072	-0.093	0.08	Fe5226	-0.09	0.076
Cr5247	-0.199	0.103	Fe5015	-0.055	0.075
Cr5265	-0.031	0.079	Hβ_o	0.05	0.071
Cr5275	-0.081	0.081	Hβ	0.089	0.071
Mn4783	-0.019	0.121	Mg *b*	-0.014	0.055
Mn4823	0.016	0.092			

this section discussing the behavior of the indices belonging to the various groups of elements. For the indices blueward of ~4800Å we do not include the galaxy FCC 164, since its spectral coverage starts around that wavelengths.

7.1 Ages and metallicities

The objects discussed here have a velocity dispersion around 30 kms^{-1}, which is similar to the objects with the lowest values in Sybilska et al. (2017). The mean age and metallicity are 10.6 Gyr, and [M/H]=-0.43, respectively. The galaxies appear to be slightly older and more metal rich than those of Sybilska et al. (2017), although their sample mostly consists of more massive galaxies. A sample that offers a better comparison is that of Toloba et al. (2014), for which all velocity dispersions lie between 20 and 40 kms^{-1}, as is the case in this paper. These authors find a mean age of 6.1 Gyr, and mean metallicity of -0.61, also slightly younger and more metal poor in comparison to our sample. These differences

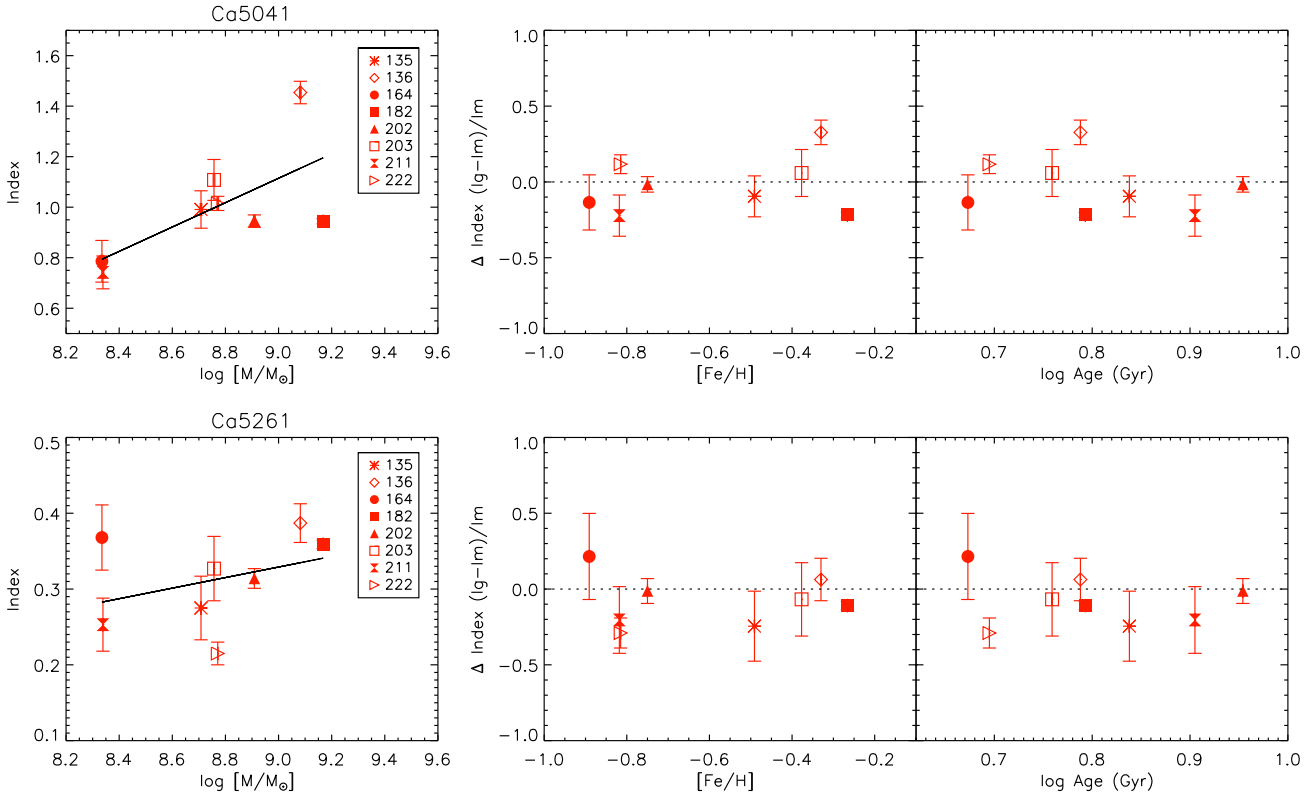

Figure 10. Comparison between index values of PEGASE.HR models and galaxies newly defined Ca lines are plotted as a function of galaxy mass (left panel), are shown in the center and right panels.

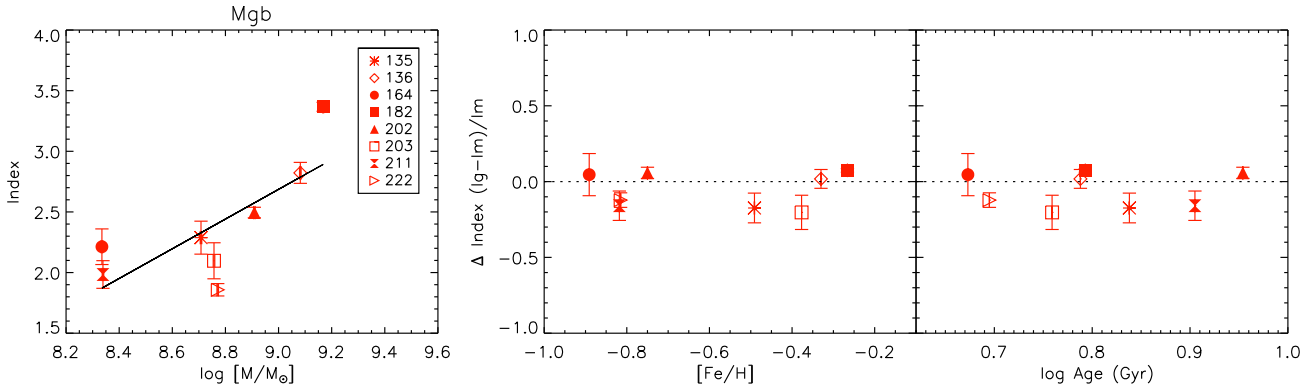

Figure 11. Comparison between index values of PEGASE.HR models and galaxies Mg line is plotted as a function of galaxy mass (left panel), is shown in the center and right panels.

could be due the fact that both the galaxies of Toloba et al. and Sybilska et al. are in Virgo, while these are in Fornax, a cluster which is more evolved in the central regions. In fact the study of Hamraz et al. (2019) shows that the scatter in the $g - z$ colour in the mass range of the dwarfs discussed here is considerably larger in Virgo than in Fornax, indicating more young stellar populations and more dust in Virgo. Beside that Kuntschner (2000) shows that all their ellipticals in Fornax cluster were consistently old, while the S0 galaxies show lower ages. However it is still possible that the result that the Virgo galaxies are less metal poor might be attributed in part to the age-metallicity degeneracy. In this case if the Virgo galaxies had the same metallicity as the ones in Fornax, their ages would have to be younger, making the difference in ages even larger. When comparing the metallicities obtained in this work with the compilation of Caldwell et al. (2003) we find lower values. Their ages are also lower, so it is possible that the age-metallicity degeneracy is at work, partly due to the fact that the employed set of indices to determine these parameters are not free from the abundance ratio effects.

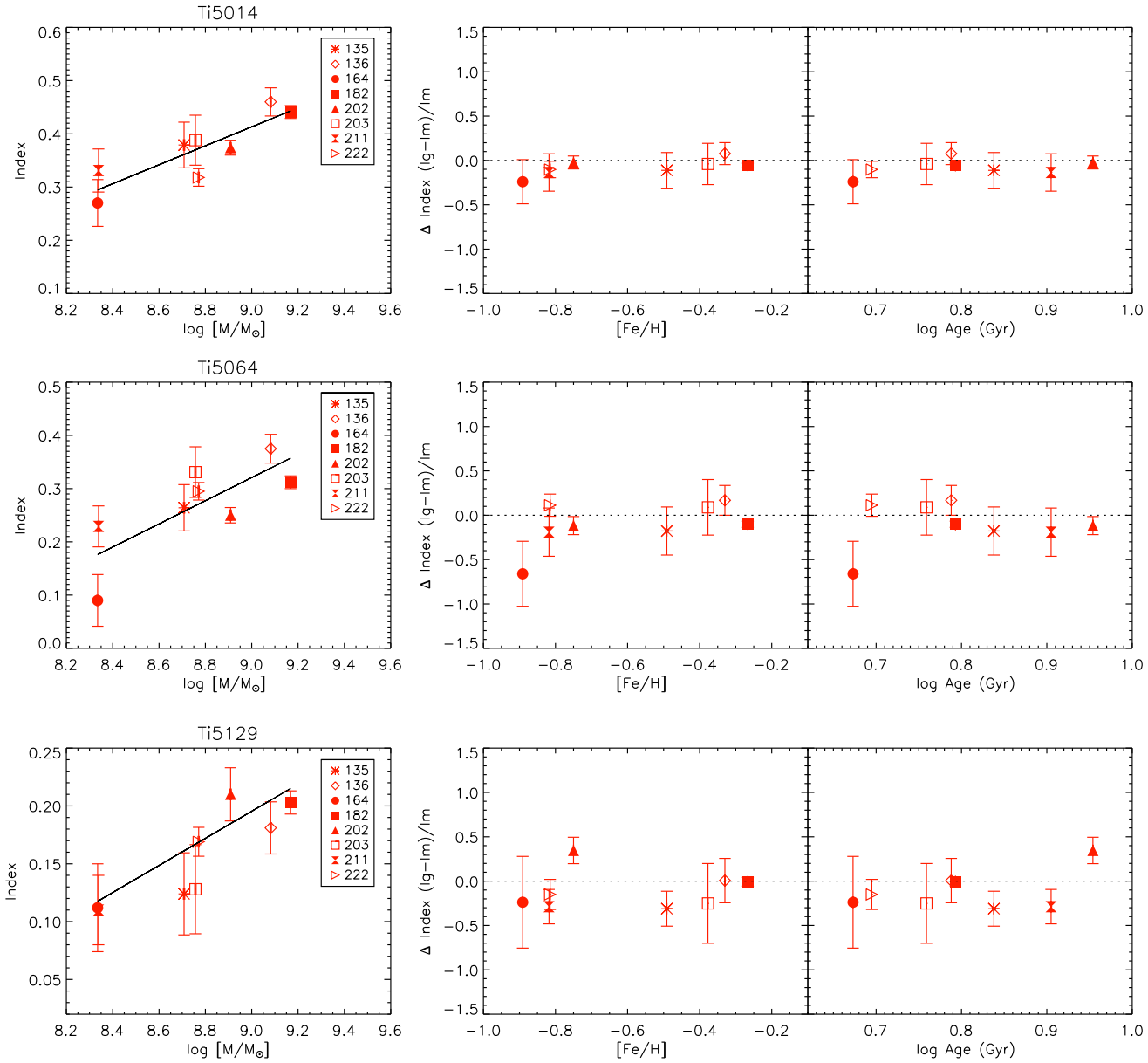

Figure 12. Comparison between index values of PEGASE.HR models and galaxies newly defined Ti lines are plotted as a function of galaxy mass (left panel), are shown in the center and right panels.

7.2 Abundance ratios of the stellar population models

The stellar population models used in this work, i.e. PEGASE.HR and MILES, are based on observed Galactic stars, mostly obtained with intermediate-size telescopes, which means that their spectra are imprinted with the abundance ratio trends of The Galaxy. In particular the Élodie library (Prugniel & Soubiran 2001) with resolution 10000, which feed the PEGASE.HR models, is composed of bright stars in the Galactic disk, although it also includes some stars at lower metallicity in the thick disk and halo. Therefore the SSP spectra computed with PEGASE.HR models also follow this pattern. Similarly, the lower resolution MILES SSP model spectra also follow the same pattern, as inferred from the abundance determinations of Milone et al. (2011) and García Pérez et al. (2021). Therefore the base models employed here have [Mg/Fe] = 0 at [Fe/H]=0, [Mg/Fe] ~ 0.2 for [Fe/H]=-0.4 and ~ 0.4 for [Fe/H]=-1.0. This has to be taken into account for discussing the abundance ratio determinations in dwarf elliptical galaxies as already shown by Sybilska et al. (2018).

7.3 The α-elements: Ca, Mg and Ti

Calcium: The two Calcium lines that are present in the covered spectral range are centered at 5041 Å and 5261 Å. We see that the measured index strengths increase with galaxy mass, being more pronounced for the line at 5041 Å. The observed index values are very close, although slightly weaker, to the ones expected from the models. Fig. 10 shows the ratio between the observed galaxy and

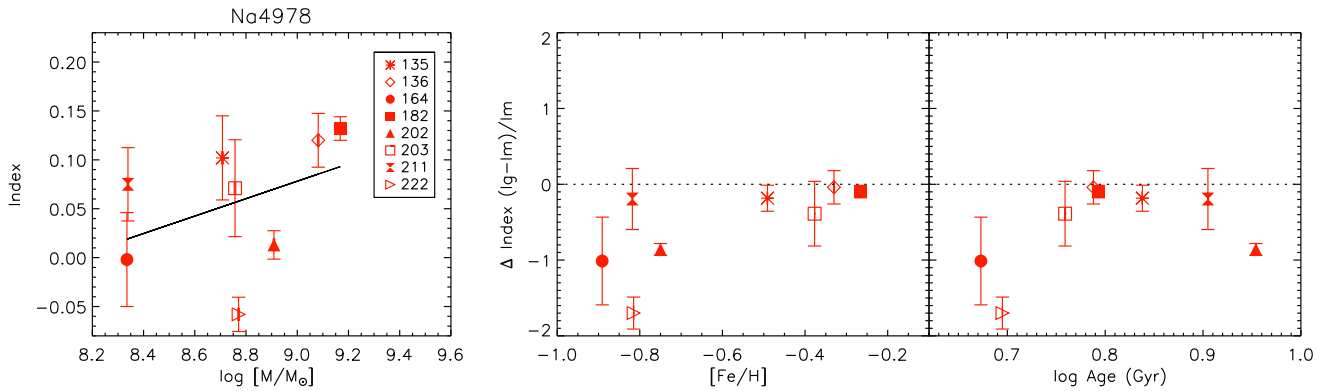

Figure 13. Comparison between index values of PEGASE.HR models and galaxies newly defined Na line is plotted as a function of galaxy mass (left panel), is shown in the center and right panels.

the ELODIE models, which were specifically selected to have the same age and metallicity as the observed galaxy. Such a difference can be attributed in part to the fact that the base models have a slightly enhanced abundance ratio of Ca, i.e. another α element, in the sub-solar metallicity regime that is characteristic of these galaxies. Therefore the relatively lower line-strengths shown by our galaxies indicate that their Ca abundance ratio is less enhanced than in the reference models and, therefore, closer to the solar-scaled value. Note that we are not attempting at matching the observed line-strengths as we are only interested in performing a qualitative assessment of the abundance ratios in these galaxies.

Magnesium: This α-element, which is produced by massive stars during the hydrostatic He burning phase, is easily measured from the Mg *b* Lick index in the observed wavelength range. Note that this is the only strong Mg line in this spectral range. We present the comparison between observed and model line-strengths in Fig. 11. Remarkably the Mg *b* shows a very strong relation with galaxy mass even at these low masses, and in such a small mass window. We find that the observed index values are slightly lower than in the models, which point to an abundance ratio that is closer to the Milky-Way abundance ratio at this subsolar metallicity regime. This result is very similar to that obtained for the Ca lines, in quite good agreement with Şen et al. (2018).

Titanium: The wavelength region observed with SAMI includes three of the stronger Ti lines. The measured index strengths are compared to the reference models in Fig. 12. We see that the three lines increase very strongly with galaxy mass as it was the case for the Mg *b* index. We see also that the three indices show similar relative deviations with respect to the models, which can be taken as a good indication of their sensitivity to the Ti abundance ratio. Ca, and Ti are mostly produced during SN II explosions, and in general they trace one another. For these galaxies we find that the Ti line-strengths are lower than the model predictions. Note that the deviations are slightly larger for the Ti5129 index, probably because this line is significantly fainter (the index values are around 0.15Å) than the other two, implying that systematic errors might have a larger effect than represented by the errorbars.

7.4 The Light odd-Z element: Na

Sodium: Na can be measured using the strong absorption features of the NaD doublet at 5890 and 5896 Å. However only the Na line at 4978 Å is available in the observed wavelength range. The index strengths observed for these dEs are lower than those predicted by the models with similar age and metallicity as shown in Fig. 13. The obtained deviation is significantly larger than those shown by the Ca, Mg and Ti lines. We see also that Na4978 shows a clear trend with [Fe/H] and age. All the results inferred for these galaxies, which are based on this line, are in good agreement with those presented in (Şen et al. 2018).

7.5 Fe-peak elements: Cr, Mn, Ni, Sc, V and Fe

Iron peak elements are the result of a complex nucleosynthesis process. Fe and Ni are produced mainly by complete explosive Si burning in the deepest layers, while Cr, Mn and V are produced mainly in the outer incomplete Si-burning layers. Sc is synthesized during explosive Oxygen / Neon burning and can be considered a transition element, intermediate between the α-elements and the iron-peak elements.

Chromium: Cr lines are represented with five lines in the observed wavelength range. All Cr lines correlate well with galaxy mass, as shown in Fig. 14. The comparison between the observed and model index strengths show that the galaxy measurements are slightly below 0 in these plots, with the largest deviations being obtained for the Cr5072. As Cr belongs to the Fe peak elements the observed deviations suggest an abundance ratio slightly below the solar-scale value.

Manganese: For Mn we use three line indices, which are shown in Fig. 15, in the observed wavelength range. Although faint all the three lines suggest that an abundance ratio slightly below solar, similarly to Cr.

Nickel: The abundance of Ni is studied by one line at 5036 Å. Fig. 16 shows that the measurements of the galaxies are lower than the values predicted by the models, leading to the same result obtained for Cr and Mn.

Scandium: Scandium is represented by one line at 5083 Å, which shows very good correlation with mass. The observed index values lie slightly lower below 0 in Fig. 17, similarly to Cr, Mn and Ni.

Vanadium: We have one, relatively strong, V line at 4924 Å, which suggest an abundance ratio rather close to solar as shown in Fig. 18.

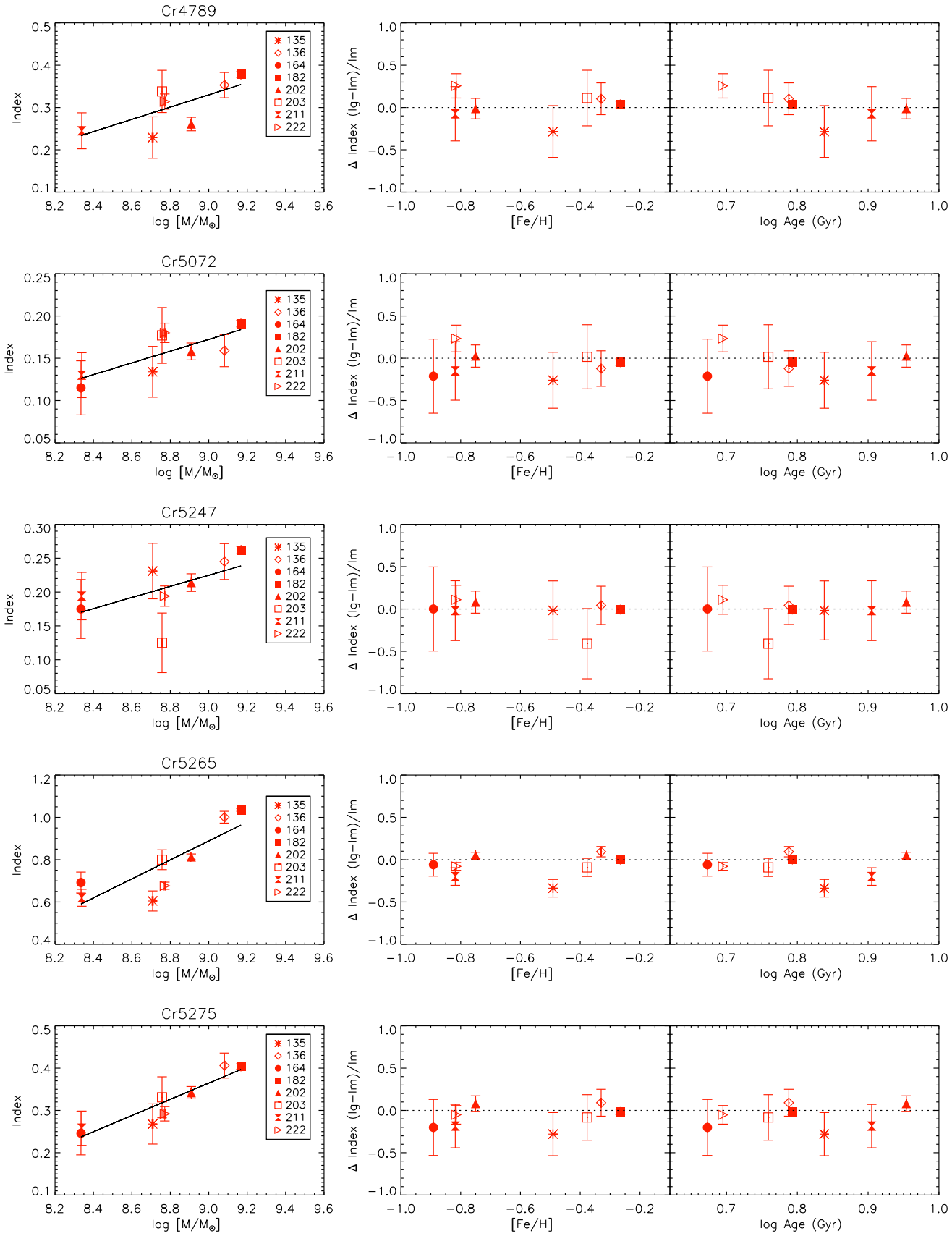

Figure 14. Comparison between index values of PEGASE.HR models and galaxies newly defined Cr lines are plotted as a function of galaxy mass (left panel), are shown in the center and right panels.

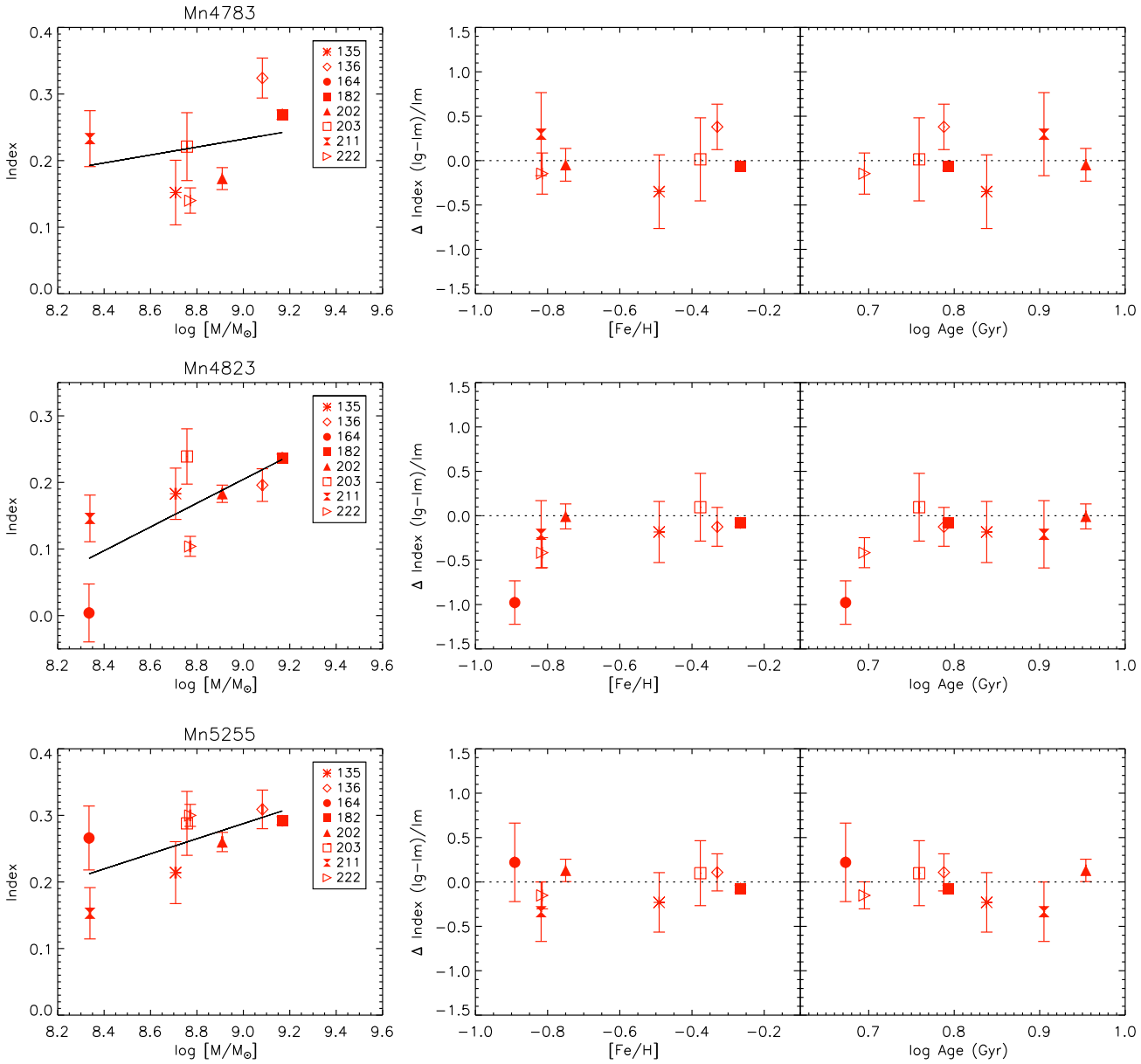

Figure 15. Comparison between index values of PEGASE.HR models and galaxies newly defined Mn lines are plotted as a function of galaxy mass (left panel), are shown in the center and right panels.

7.6 Neutron capture elements: Ba, Y, Nd

Heavy elements are those with atomic number higher than 30, like Yttrium (Y), Barium (Ba) and Neodymium (Nd). They can only be produced by neutron capture elements that are exposed to high neutron flux. Iron peak elements are the most efficient seeds to capture neutrons to create heavier elements. There are two main paths to form these elements: the s-process (or slow process) and the r-process (rapid process).

The s-process occurs when the neutron flux is not very high, so that the intervals between neutron captures are long compared to the beta decay characteristic timescale of an unstable nucleus.

Tolstoy et al. (2009) compare Ba, Y and Eu abundances in Local Group dwarf Spheroidals and in the Milky Way. In dSphs, the early evolution of all neutron-capture elements is dominated by the r-process, after which the s-process starts taking over from the r-process. The metallicity of switch from r- to s-process is the same as the [α/Fe] knee ([Fe/H] ~ -1.8), i.e. much lower than in the Milky Way. In the latter, Ba and Y are dominated by the r-process for [Fe/H] $\leq$ -2.0, while the s-process dominates at higher metallicities, for instance more than 80% of the solar Ba is originating from the s-process.

Barium: is represented by one line, Ba2, at 4895 Å. *Yttrium:* is well represented by a line at 4854 Å in our dwarf galaxies. *Neodymium:* can be measured by a line centered at 5192 Å. All heavy elements are found to have abundances slightly lower than the solar-scale value as shown in Fig 19.

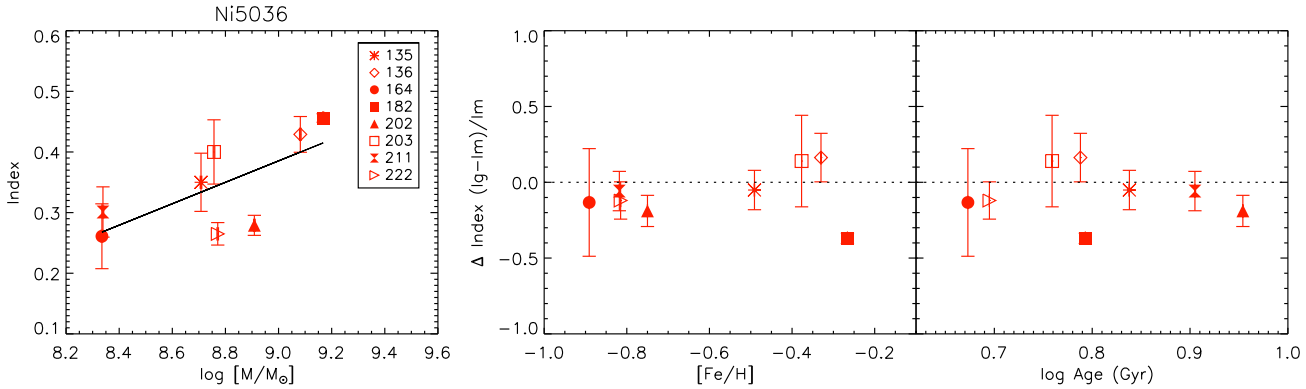

Figure 16. Comparison between index values of PEGASE.HR models and galaxies newly defined Ni line is plotted as a function of galaxy mass (left panel), is shown in the center and right panels.

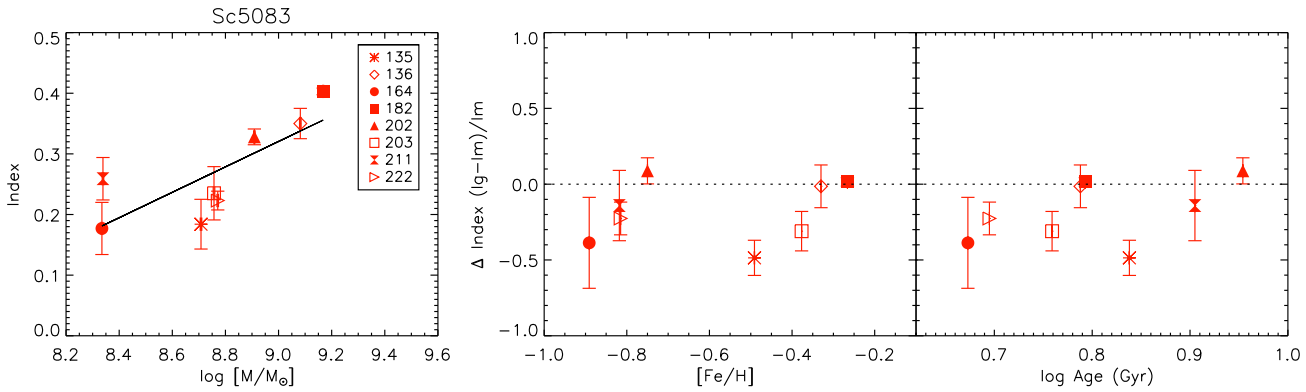

Figure 17. Comparison between index values of PEGASE.HR models and galaxies newly defined Sc line is plotted as a function of galaxy mass (left panel), is shown in the center and right panels.

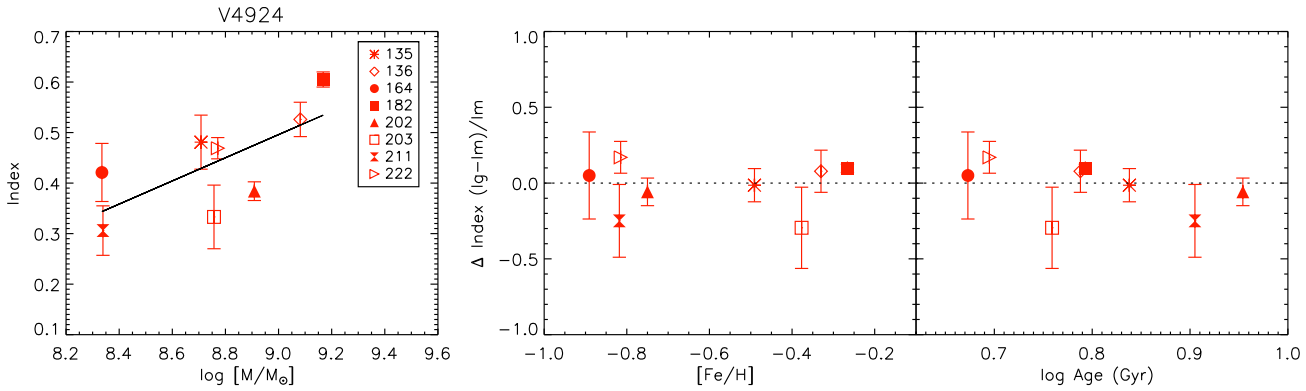

Figure 18. Comparison between index values of PEGASE.HR models and galaxies newly defined V line is plotted as a function of galaxy mass (left panel), is shown in the center and right panels.

8 DISCUSSION

The main results from this paper are summarized in Fig. 20, where we show the proxy for the abundance ratios for the 11 elements derived here. For comparison we also provide the "true" abundance ratio estimates for more massive ellipticals with very different velocity dispersion values by Conroy et al. (2014). We note that the derived abundance ratio proxies for our galaxies as relative index deviations with respect to the reference base SSP models. These models are fed with empirical stars and therefore follow the Milky-Way abundance pattern, which is represented in Fig. 20 by a "0.0" value in its left vertical axis. It is worth recalling that this reference valued does not mean solar-scaled abundance (which is only true at solar metallicity). We do not calibrate these deviations in terms of abundance element ratios. In contrast the right vertical axis indicates the abundance ratio values for the gEs shown in this

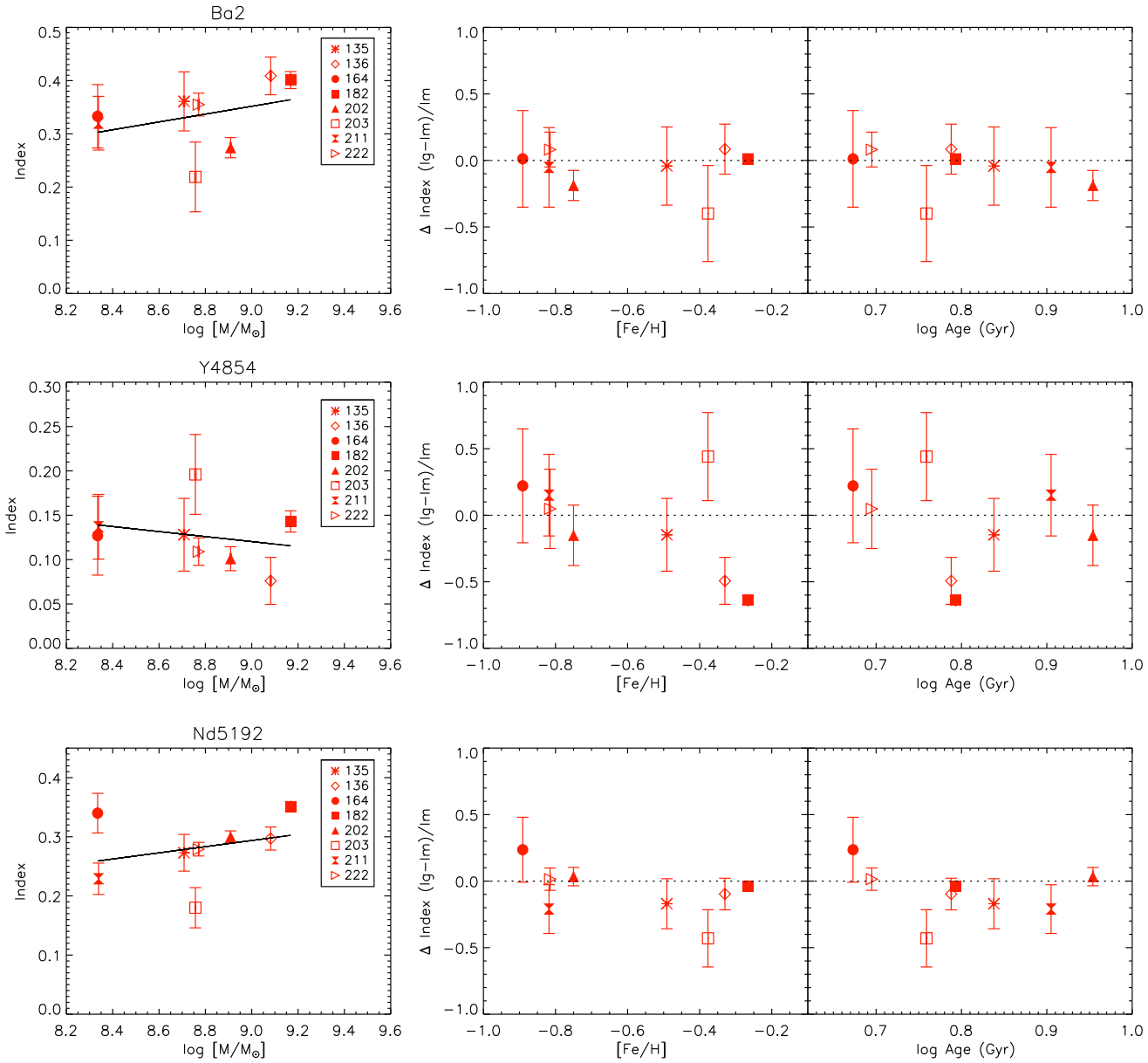

Figure 19. Comparison between index values of PEGASE.HR models and galaxies newly defined heavy elements lines are plotted as a function of galaxy mass (left panel), are shown in the center and right panels.

figure. However, having these two estimates in the same plot allow us to compare visually these trends. It is worth recalling that such comparison is provided with the only purpose of assessing the difference in the derived abundance trends between these three families of galaxies, rather than an in-depth quantitative analysis of the their true abundances.

For our galaxies we find that the abundance ratio proxies of all elements are either below or close to the solar-scale value. This means that these dwarf galaxies form their stars slowly, like in the disk of the Milky Way. The results obtained here for Mg and Ca are in rather good agreement with the ones published in Şen et al. (2018). This behavior fits nicely on a trend with increasing mass, from dwarfs, through Milky-way type galaxies, to the most massive giant galaxies, as analysed by Conroy et al. (2014). Galaxies with $\sigma \sim 100$ kms^{-1} have abundance ratios that are close to solar, while in massive galaxies the α-elements are enhanced, together with a few other elements (see Conroy et al. 2014). In particular, Na shows a different relation, being significantly lower than solar for dwarfs as compared to the solar-scale value, and much higher for giant ellipticals (e.g. Smith et al. 2015; La Barbera et al. 2017).

We can make a few remarks for some specific elements. We find that [Mn/Fe] seems to be a bit lower than abundance ratios of other Fe-peak elements. This result is likely consistent with the [Mn/Fe] ratios derived for Galactic stars in the sub-solar metallicity regime of our dEs, i.e. [Mn/Fe]∼-0.2 around [Fe/H]∼-0.5 Gratton 1989; McWilliam et al. 2003). The latter reference also shows that in the Galactic bulge and in the Sagittarius dwarf the [Mn/Fe] abundance is once again about 0.2 lower than the solar-scale value. Although

the abundance of V has not yet been well determined, it is still thought that [V/Fe] is around ~ 0.0 at all metallicities (Gratton & Sneden 1991). If the Mn deficiencies are due to a neutron excess dependence, then V and Sc are also expected to follow the same trend, as is inferred for the present sample of dEs, although we only rely on a single line in this study.

Na is a very interesting element that is produced in the interiors of massive stars depending on the neutron excess. This means that it depends on the initial heavy element abundance in the star. We find that Na line strengths show low values compared to the models in the dEs. These results are in good agreement with the results of Şen et al. (2018), which show that for Virgo dEs the [Na/Fe] is under-abundant with respect to the solar-scale value. Note that this is in sharp contrast with the abundance found for giant ellipticals, which show strongly overabundant [Na/Fe] abundance ratios (e.g. Conroy et al. 2014; La Barbera et al. 2017). This abundance ratio also shows a strong correlation with galaxy mass.

The similarities with disk-like abundance ratios may suggest that dEs originate from star forming galaxies with rather slow formation. Given that dEs are mostly found in dense environments (e.g. Binggeli et al. 1988), where star forming galaxies are scarce, point to late types spirals or star forming dwarfs (e.g. dwarf irregulars), losing their interstellar medium when entering the cluster through ram pressure stripping (see e.g. Boselli & Gavazzi 2014; Choque-Challapa et al. 2019). It is in principle also possible that galaxy interactions, i.e., galaxy harassment (Moore et al. 1996) causes this transformation, but in such a case it would be expected considerable changes in the properties of dEs as a function of position in the cluster, which have not been seen up to now (e.g. Venhola et al. 2019). The scenario of star forming dwarfs transforming into quiescent dEs agrees with recent kinematic results of Scott et al. (2020). These authors show that the rotational support in dEs is similar or slightly lower than in star forming dwarfs. No strong relation was found between the rotational support and the cluster-centric distance. If dEs form from late-type spirals, such as Sd or Sm galaxies, a considerable amount of angular momentum has to be lost, which points to galaxy harassment as the process that is responsible for this transformation.

We will discuss the star formation histories of our present sample of galaxies and other dEs in an upcoming paper (Romero et al., in preparation). The results obtained here indicate long star formation time scales for these galaxies.

9 CONCLUSIONS

- This is the first time that an attempt has been made to determine abundance ratio proxies of many elements in unresolved dwarf galaxies outside the Local Group. It was done using a sample of dE galaxies, observed using SAMI at the AAT at a resolution of ~ 5000. These abundance proxies must be understood as relative index deviations with respect to the model predictions that follow the Milky-Way abundance pattern.
- We analysed the absorption line-strengths of our new high resolution system of indices for a sample of 8 Fornax dwarf galaxies, which had been classified as cluster members in Venhola et al. (2019).
- Taking advantage of the high resolution spectral data and low velocity dispersion (40 kms^{-1}) of these galaxies we were able to measure the new high resolution indices with our SAMI data and compare the obtained index values to the predictions of the PEGASE.HR stellar population models. We derive abundance proxies for 11 elements and compare them with the abundance ratios of massive galaxies by Conroy et al. (2014) as a function of mass as traced by their velocity dispersion. We find that the dwarf galaxies in our sample have abundance ratios that are close to solar-scale or slightly below this value. This pattern is consistent with an extrapolation of the abundances of massive galaxies (Conroy et al. 2014) to lower masses.
- We find that these dwarf galaxies have [Na/Fe] abundance ratios that are considerably lower than the solar-scale value. This result is in good agreement with Virgo dEs, which show that [Na/Fe] is under-abundant with respect to the solar element partition (Şen et al. 2018) .
- This work indicates the large potential for future studies of low mass stellar systems, with powerful instruments, such as X-Shooter on the VLT.

ACKNOWLEDGEMENTS

Ş. Ş. (Aydemir) acknowledges support from grant 2218-National Postdoctoral Research Fellowship Program for Turkish Citizens under project number 118C553 and application number 1929B012100279 from the The Scientific and Technological Research Council of Turkey (TUBITAK). RFP acknowledges financial support from the European Union's Horizon 2020 research and innovation program under the Marie Sklodowska-Curie grant agreement No. 721463 to the SUNDIAL ITN network. A.V. acknowledges support from grants PID2019-107427GB-C32 from the Spanish Ministry of Science, Innovation and Universities (MCIU).

DATA AVAILABILITY

The raw data used in this paper, from the SAMI instrument, are available from the AAT data archive. The reduced data are cubes are available upon request, and will be made available in the near future together with a future paper on the star formation histories of dwarf galaxies in the Fornax Cluster.

REFERENCES

Allen J. T., et al., 2015, MNRAS, 451, 2780
Barazza F. D., Binggeli B., Jerjen H., 2002, A&A, 391, 823
Bidaran B., et al., 2020, MNRAS,
Binggeli B., Sandage A., Tammann G. A., 1988, ARA&A, 26, 509
Bland-Hawthorn J., et al., 2011, Optics Express, 19, 2649
Boselli A., Gavazzi G., 2014, A&ARv, 22, 74
Bryant J. J., O'Byrne J. W., Bland-Hawthorn J., Leon-Saval S. G., 2011, MNRAS, 415, 2173
Bryant J. J., Bland-Hawthorn J., Fogarty L. M. R., Lawrence J. S., Croom S. M., 2014, MNRAS, 438, 869
Caldwell N., Rose J. A., Concannon K. D., 2003, AJ, 125, 2891
Caon N., Capaccioli M., D'Onofrio M., 1993, MNRAS, 265, 1013
Cardiel N., 1999, PhD thesis, , Universidad Complutense de Madrid, Spain, (1999)
Cardiel N., Gorgas J., Sánchez-Blázquez P., Cenarro A. J., Pedraz S., Bruzual G., Klement J., 2003, A&A, 409, 511
Cervantes J. L., Vazdekis A., 2009, MNRAS, 392, 691
Choque-Challapa N., Smith R., Candlish G., Peletier R., Shin J., 2019, MNRAS, 490, 3654
Cid Fernandes R., Mateus A., Sodré L., Stasińska G., Gomes J. M., 2005, MNRAS, 358, 363
Coelho P., Barbuy B., Meléndez J., Schiavon R. P., Castilho B. V., 2005, A&A, 443, 735

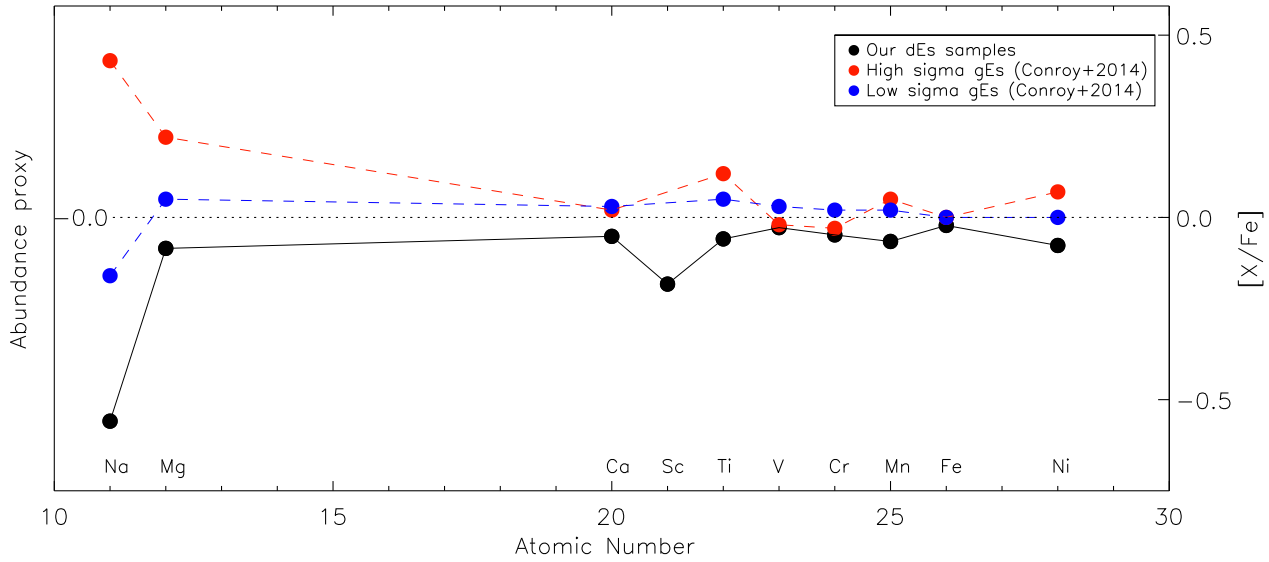

Figure 20. Summary of the abundance trends derived here from our work and low- and high- velocity dispersion gEs (Conroy et al. 2014). Note that we indicate the abundance ratio values in the right vertical axis, which apply to the two gEs samples shown here. The abundance proxy estimates for our dwarf galaxies are reflected in the left vertical axis, where we indicate only the relative non-calibrated index deviations with respect to the reference base SSP models, represented by the 0.0 value.

Conroy C., Graves G. J., van Dokkum P. G., 2014, ApJ, 780, 33
Croom S. M., et al., 2012, MNRAS, 421, 872
De Rijcke S., Dejonghe H., Zeilinger W. W., Hau G. K. T., 2003, A&A, 400, 119
Ferrarese L., et al., 2006, ApJS, 164, 334
García Pérez A. E., et al., 2021, MNRAS,
Geha M., Guhathakurta P., van der Marel R. P., 2003, AJ, 126, 1794
Gorgas J., Pedraz S., Guzmán R., Cardiel N., González J. J., 1997, ApJ, 481, L19
Graham A. W., Guzmán R., 2003, AJ, 125, 2936
Gratton R. G., 1989, A&A, 208, 171
Gratton R. G., Sneden C., 1991, A&A, 241, 501
Green A. W., et al., 2018, MNRAS, 475, 716
Hamraz E., Peletier R. F., Khosroshahi H. G., Valentijn E. A., den Brok M., Venhola A., 2019, A&A, 625, A94
Janz J., et al., 2012, ApJ, 745, L24
Janz J., et al., 2014, ApJ, 786, 105
Jerjen H., Kalnajs A., Binggeli B., 2000, A&A, 358, 845
Jones L. A., Worthey G., 1995, ApJ, 446, L31
Jordán A., et al., 2007, ApJS, 171, 101
Koleva M., de Rijcke S., Prugniel P., Zeilinger W. W., Michielsen D., 2009, MNRAS, 396, 2133
Koleva M., Prugniel P., de Rijcke S., Zeilinger W. W., 2011, MNRAS, 417, 1643
Kormendy J., 1985, ApJ, 295, 73
Kuntschner H., 2000, MNRAS, 315, 184
Kuntschner H., Davies R. L., 1998, MNRAS, 295, L29
Kuntschner H., et al., 2010, MNRAS, 408, 97
La Barbera F., Vazdekis A., Ferreras I., Pasquali A., Allende Prieto C., Röck B., Aguado D. S., Peletier R. F., 2017, MNRAS, 464, 3597
Le Borgne D., Rocca-Volmerange B., Prugniel P., Lançon A., Fioc M., Soubiran C., 2004, A&A, 425, 881
Lisker T., Grebel E. K., Binggeli B., 2006, AJ, 132, 497
Lisker T., Grebel E. K., Binggeli B., Glatt K., 2007, ApJ, 660, 1186
McWilliam A., Rich R. M., Smecker-Hane T. A., 2003, ApJ, 592, L21
Michea J., Pasquali A., Smith R., Calderón-Castillo P., Grebel E. K., Peletier R. F., 2022, arXiv e-prints, p. arXiv:2205.06281
Michielsen D., et al., 2008, MNRAS, 385, 1374
Milone A. D. C., Sansom A. E., Sánchez-Blázquez P., 2011, MNRAS, 414, 1227
Moore B., Katz N., Lake G., Dressler A., Oemler A., 1996, Nature, 379, 613
Nelan J. E., Smith R. J., Hudson M. J., Wegner G. A., Lucey J. R., Moore S. A. W., Quinney S. J., Suntzeff N. B., 2005, ApJ, 632, 137
Paudel S., Lisker T., Kuntschner H., Grebel E. K., Glatt K., 2010, MNRAS, 405, 800
Penny S. J., et al., 2016, MNRAS, 462, 3955
Penny S. J., et al., 2018, MNRAS, 476, 979
Prugniel P., Soubiran C., 2001, A&A, 369, 1048
Prugniel P., Soubiran C., 2004, ArXiv Astrophysics e-prints,
Ryś A., Falcón-Barroso J., van de Ven G., 2013, MNRAS, 428, 2980
Ryś A., van de Ven G., Falcón-Barroso J., 2014, MNRAS, 439, 284
Ryś A., Koleva M., Falcón-Barroso J., Vazdekis A., Lisker T., Peletier R., van de Ven G., 2015, MNRAS, 452, 1888
Sánchez-Blázquez P., Gorgas J., Cardiel N., Cenarro J., González J. J., 2003, ApJ, 590, L91
Sandage A., Binggeli B., 1984, AJ, 89, 919
Scott N., et al., 2018, MNRAS, 481, 2299
Scott N., et al., 2020, MNRAS, 497, 1571
Searle L., Sargent W. L. W., 1972, ApJ, 173, 25
Sharp R., et al., 2015, MNRAS, 446, 1551
Skillman E. D., Kennicutt R. C., Hodge P. W., 1989, ApJ, 347, 875
Smith R., et al., 2015, MNRAS, 454, 2502
Su A. H., et al., 2021, A&A, 647, A100
Sybilska A., et al., 2017, MNRAS, 470, 815
Sybilska A., Kuntschner H., van de Ven G., Vazdekis A., Falcón-Barroso J., Peletier R. F., Lisker T., 2018, MNRAS, 476, 4501
Thomas D., Maraston C., Bender R., Mendes de Oliveira C., 2005, ApJ, 621, 673
Toloba E., et al., 2014, ApJS, 215, 17
Toloba E., et al., 2015, ApJ, 799, 172
Tolstoy E., Hill V., Tosi M., 2009, ARA&A, 47, 371
Trager S. C., Faber S. M., Worthey G., González J. J., 2000, AJ, 120, 165
Vazdekis A., 1999, ApJ, 513, 224
Vazdekis A., 2001, Ap&SS, 276, 839
Vazdekis A., Peletier R. F., Beckman J. E., Casuso E., 1997, ApJS, 111, 203
Vazdekis A., Trujillo I., Yamada Y., 2004, ApJ, 601, L33
Vazdekis A., Sánchez-Blázquez P., Falcón-Barroso J., Cenarro A. J., Beasley M. A., Cardiel N., Gorgas J., Peletier R. F., 2010, MNRAS, 404, 1639

Table A1. INDEX DEFINITIONS.

Name	Index Bandpass Å	Blue Continuum Å	Red Continuum Å
Ba2	4930.000–4935.800	4894.400–4896.800	4948.600–4951.800
Ca5041	5036.200–5043.740	5032.720–5034.790	5056.820–5059.460
Ca5261	5259.925–5263.260	5257.400–5259.500	5277.310–5279.410
Cr4789	4787.350–4791.120	4768.880–4771.080	4793.450–4795.700
Cr5072	5071.095–5073.570	5056.820–5059.460	5092.920–5095.800
Cr5247	5244.700–5248.495	5236.250–5238.250	5256.200–5259.200
Cr5265	5263.700–5268.340	5257.400–5259.500	5277.310–5279.410
Cr5275	5273.700–5277.600	5257.400–5259.500	5277.310–5279.410
Fe4891	4889.125–4893.040	4856.250–4858.250	4893.800–4896.200
Fe4920	4914.425–4921.850	4894.400–4896.800	4948.600–4951.800
Fe5226	5219.800–5230.240	5212.400–5214.500	5236.250–5238.250
Mn4783	4781.500–4785.560	4768.880–4771.080	4793.450–4795.700
Mn4823	4822.420–4825.780	4814.600–4820.200	4844.500–4846.900
Mn5255	5253.200–5257.260	5236.250–5238.250	5256.200–5259.200
Na4978	4976.300–4979.780	4948.730–4952.190	4986.600–4988.760
Nd5192	5190.940–5193.530	5174.500–5178.500	5198.540–5201.760
Ni5036	5034.440–5037.420	5032.720–5034.790	5056.820–5059.460
Sc5083	5081.150–5084.920	5056.820–5059.460	5092.920–5095.800
Ti5014	5012.350–5016.120	5002.400–5005.100	5032.260–5034.330
Ti5064	5063.380–5067.280	5056.820–5059.460	5092.920–5095.800
Ti5129	5127.800–5130.680	5118.800–5121.000	5143.710–5147.140
V4924	4922.000–4927.480	4894.400–4896.800	4948.600–4951.800
Y4854	4853.680–4856.410	4844.800–4846.900	4856.500–4858.500

Venhola A., et al., 2018, A&A, 620, A165
Venhola A., et al., 2019, A&A, 625, A143
Walcher C. J., Coelho P., Gallazzi A., Charlot S., 2009, MNRAS, 398, L44
Worthey G., 1994, ApJS, 95, 107
Worthey G., Ottaviani D. L., 1997, ApJS, 111, 377
Worthey G., Dorman B., Jones L. A., 1996, AJ, 112, 948
Worthey G., Danilet A. B., Faber S. M., 2014, A&A, 561, A36
Şen Ş., et al., 2018, MNRAS, 475, 3453
den Brok M., et al., 2011, MNRAS, 414, 3052

APPENDIX A: TABLE

Table A2. Age-metallicity dependence. Column 1: index name. Columns 2 and 3: metallicity and age dependence. Columns 4: indicating age or metallicity indicator. The elements H and Mg are presented here as a reference elements; a= age indicator, m=metallicity indicator, a*=more affected by age, m*=more affected by metallicity, blank ones are affected by both.

Index	A_i	B_i	Indicator
Ba2	0.362 ±0.138	0.532 ±0.102	a*
Ca5041	0.399 ±0.123	0.472 ±0.123	...
Ca5261	0.414 ±0.089	0.473 ±0.089	...
Cr4789	0.502 ±0.169	0.530 ±0.193	...
Cr5072	0.460 ±0.130	0.504 ±0.143	...
Cr5247	0.928 ±0.111	1.824 ±1.019	...
Cr5265	0.443 ±0.124	0.485 ±0.132	...
Cr5275	0.411 ±0.127	0.347 ±0.142	m*
Fe4891	0.552 ±0.238	0.747 ±0.164	m*
Fe4920	0.475 ±0.179	0.507 ±0.180	...
Fe5226	0.482 ±0.097	0.561 ±0.100	...
Mn4783	0.715 ±0.166	0.719 ±0.273	...
Mn4823	0.491 ±0.183	0.506 ±0.160	...
Mn5255	0.556 ±0.135	0.500 ±0.178	...
Na4978	0.675 ±0.151	0.767 ±0.338	...
Nd5192	0.395 ±0.111	0.501 ±0.103	m*
Ni5036	0.417 ±0.122	0.466 ±0.132	...
Sc5083	0.435 ±0.127	0.560 ±0.118	a*
Ti5014	0.385 ±0.161	0.567 ±0.133	a*
Ti5064	0.442 ±0.088	0.648 ±0.080	a*
V4924	0.425 ±0.179	0.382 ±0.176	m*
Y4854	0.918 ±0.474	0.908 ±0.401	...
Mg b	0.760 ±0.192	0.438 ±0.161	m
Hβ	0.163 ±0.075	0.557 ±0.050	a
Hβ_o	0.061 ±0.032	0.456 ±0.019	a

Table A3. Abundance ratio proxies for a number of elements.

Name	Abundance proxy
Na	-0.6
Mg	-0.1
Ca	-0.1
Sc	-0.2
Ti	-0.1
V	0.0
Cr	0.0
Mn	-0.1
Fe	0.0
Ni	-0.1

APPENDIX B: ALL FIGURES FOR THE BEHAVIOUR OF THE INDICES AS A FUNCTION OF METALLICITY, AGE AND SPECTRAL RESOLUTION

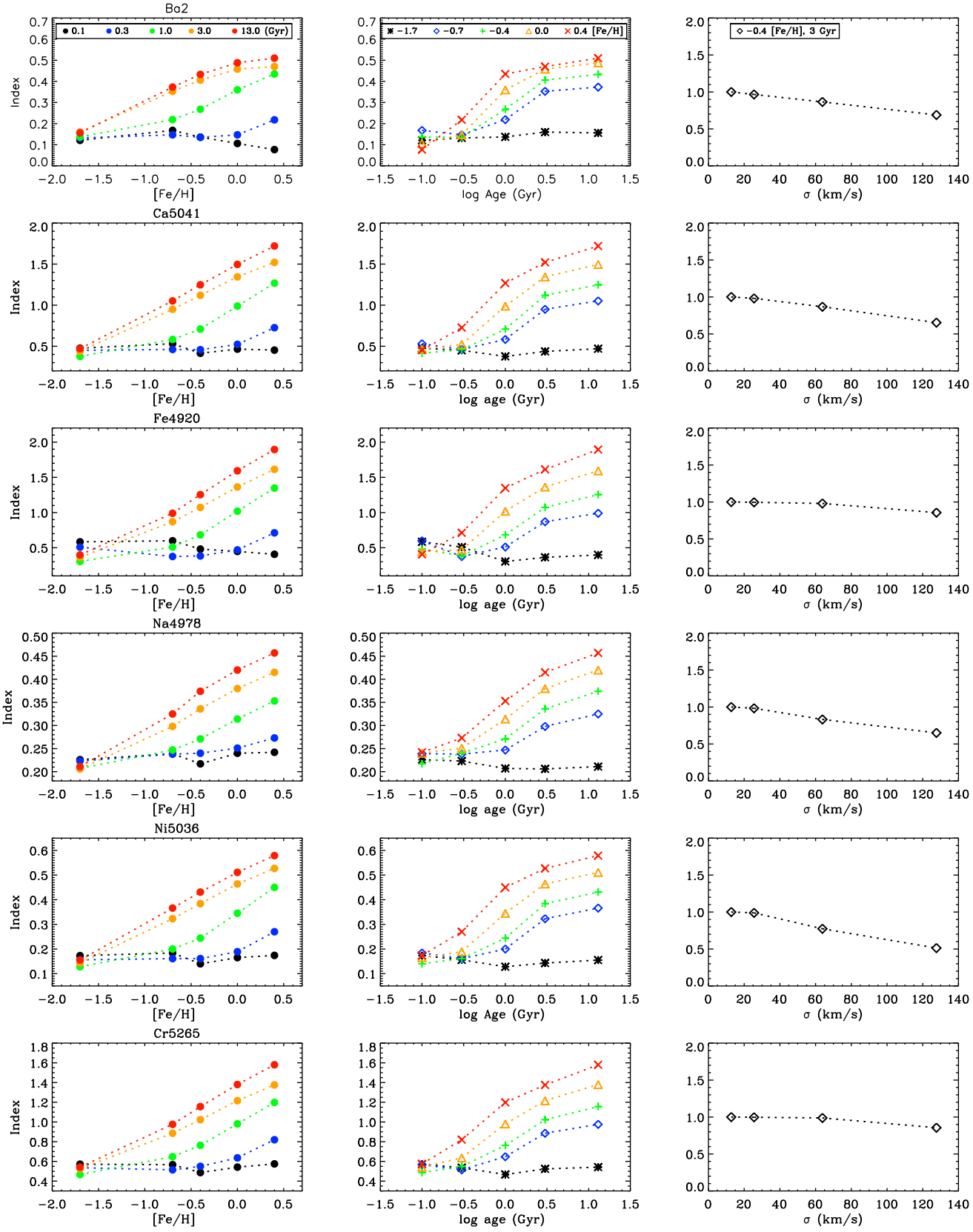

Figure B1. Behaviour of the indices as a function of metallicity, age and spectral resolution. On the left is shown the indices vs. metallicity ([Fe/H]= -1.7, -0.7, -0.4, 0.0, 0.4); each age is shown as a circle with different colour. In the middle is shown the behaviour of indices vs. age (0.1, 0.3, 1, 3, 13 Gyr); each metallicity has a different symbol with different colour. The left and middle panels have been calculated for σ= 25 km s^{-1}. On the right is shown the behaviour of indices as a function of velocity dispersion (with σ= 10-130 km s^{-1}). Their dependence on σ are given for the case of a model with t = 3 Gyr and [Fe/H]= -0.4, typical for the dwarf galaxies discussed in section 5.1. Here 6 example indices are shown.

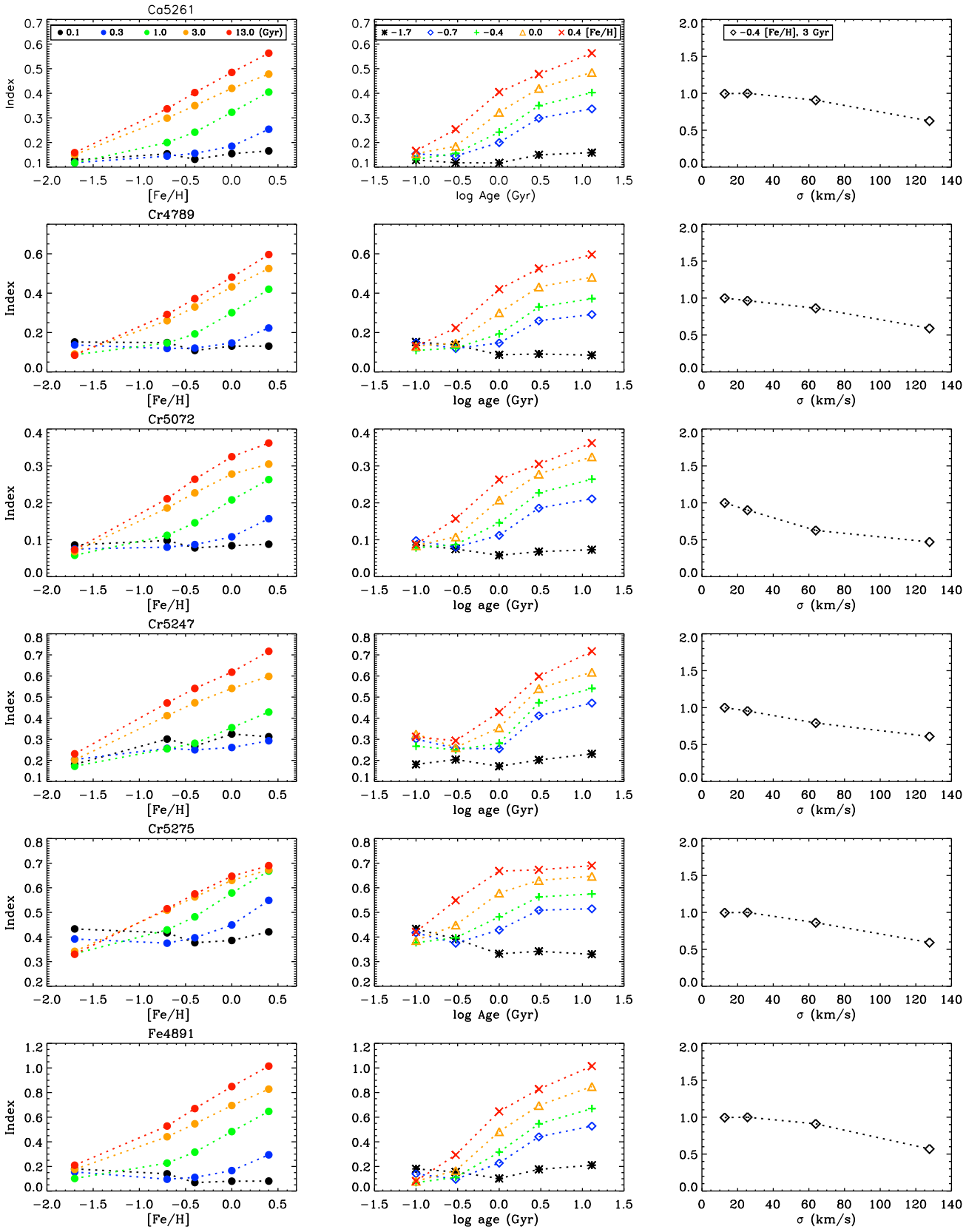

Figure B2. Same as Figure B1, now for the indices: Ca5261, Cr4789, Cr5072, Cr5247, Cr5275 and Fe4891.

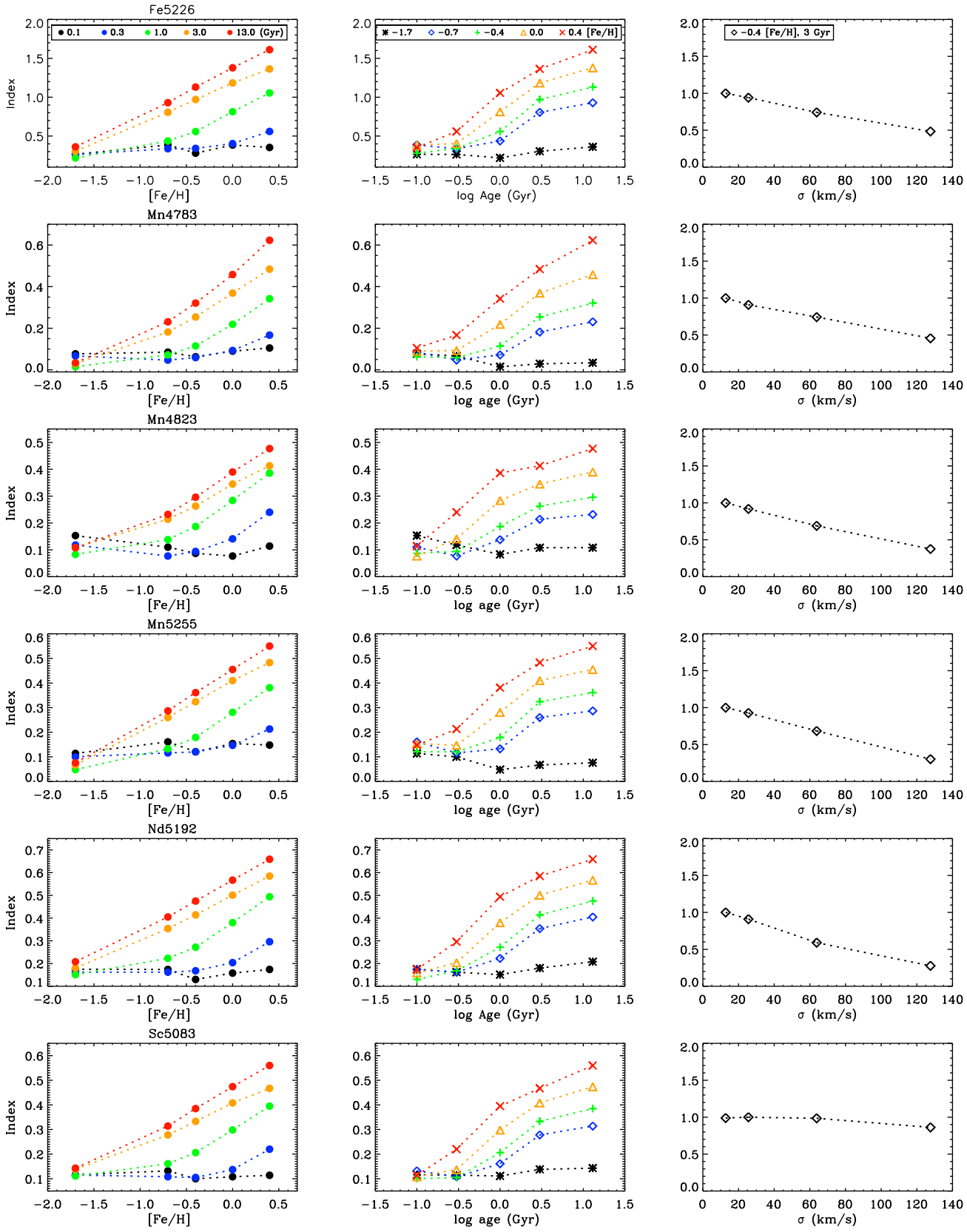

Figure B3. Same as Figure B1, now for the indices: Fe5226, Mn4783, Mn4823, Mn5255, Nd5192 and Sc5083.

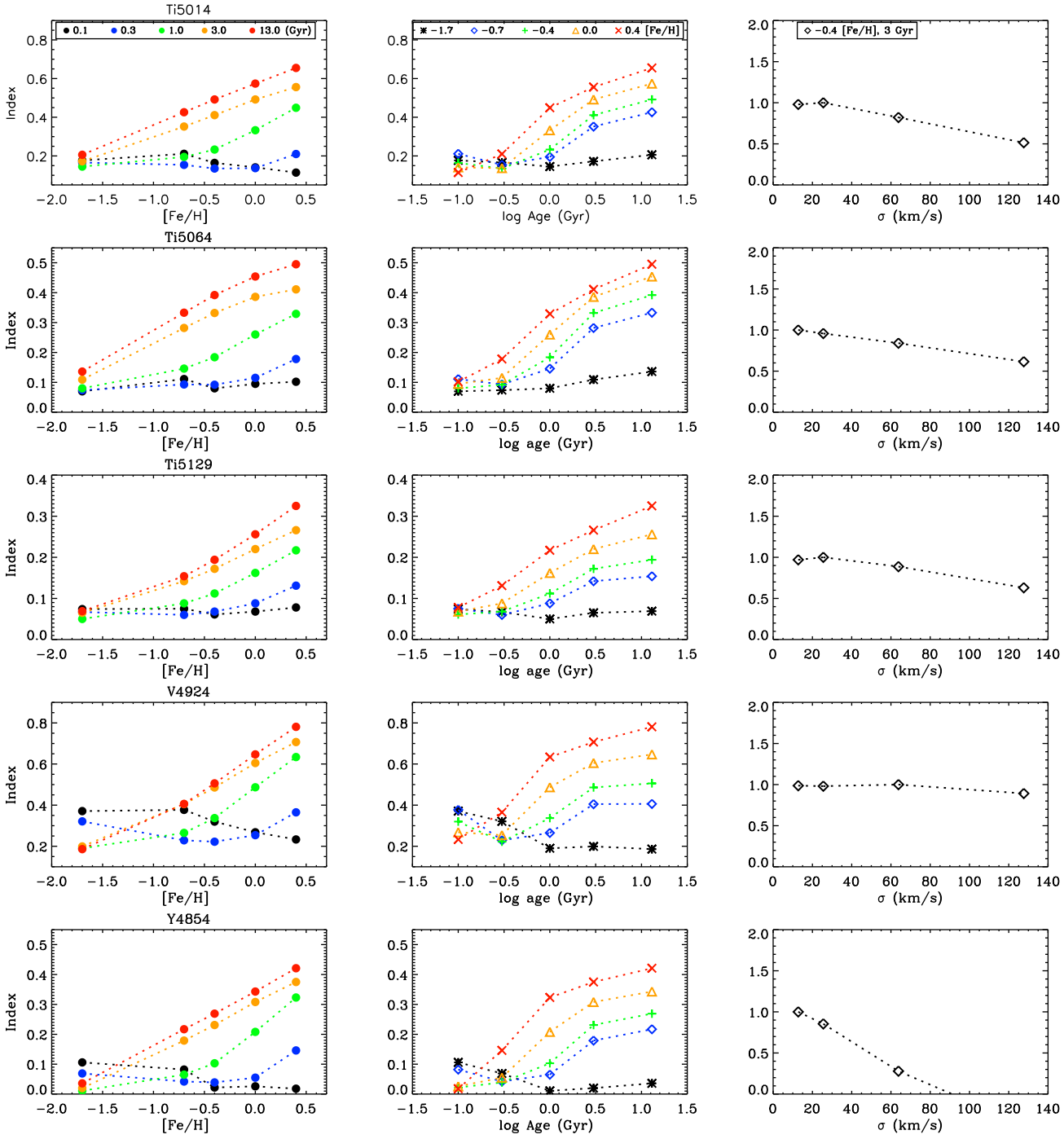

Figure B4. Same as Figure B1, now for the indices: Ti5014, Ti5064, Ti5129, V4924 and Y4854.

APPENDIX C: ALL FIGURES FOR THE BEHAVIOUR OF THE INDICES AS A FUNCTION OF EFFECTIVE TEMPERATURE, SURFACE GRAVITY AND METALLICITY

We measured the indices of Elodie stars with σ= 25 kms^{-1} to understand how the line indices change as a function of effective temperature (log $T_{\rm eff}$), surface gravity (log g) and metallicity ([Fe/H]). They are shown in Fig. C1-Fig. C4.

APPENDIX D: FIGURE FOR THE COMPARISON OF AGE AND METALLICITY DEPENDENCE FOR ELEMENTS

Figure D1 shows the values of A$_i$ and B$_i$ for each index i grouped per element.

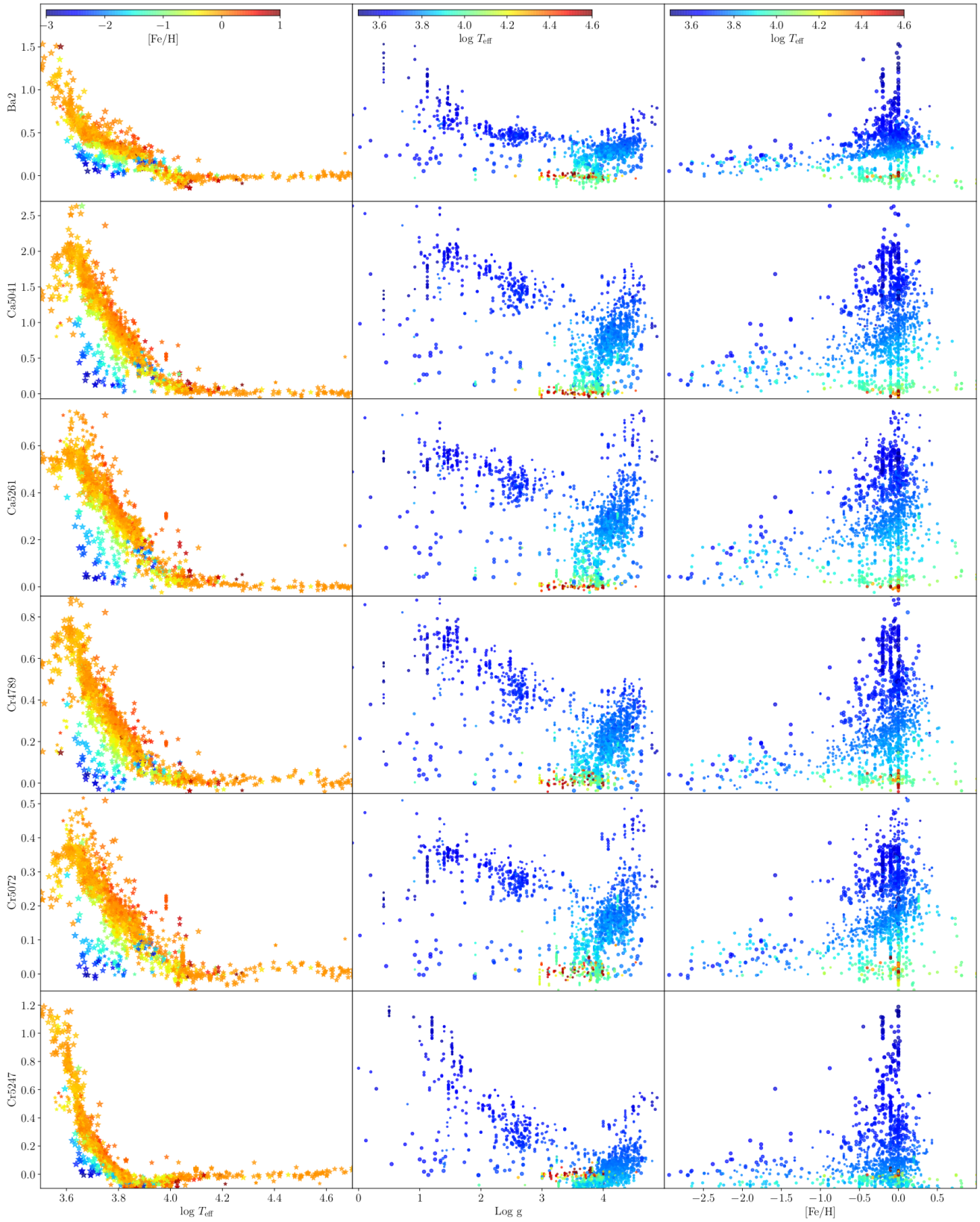

Figure C1. Indices as a function of effective temperature (log $T_{\rm eff}$), surface gravity (log g) and metallicity ([Fe/H]) shown for all the Elodie stars. The ELODIE library is a stellar database of 1959 spectra for 1503 stars with atmospheric parameters: $T_{\rm eff}$ from 3000 K to 60000 K, log g from -0.3 to 5.9 and [Fe/H] from -3.2 to +1.4.

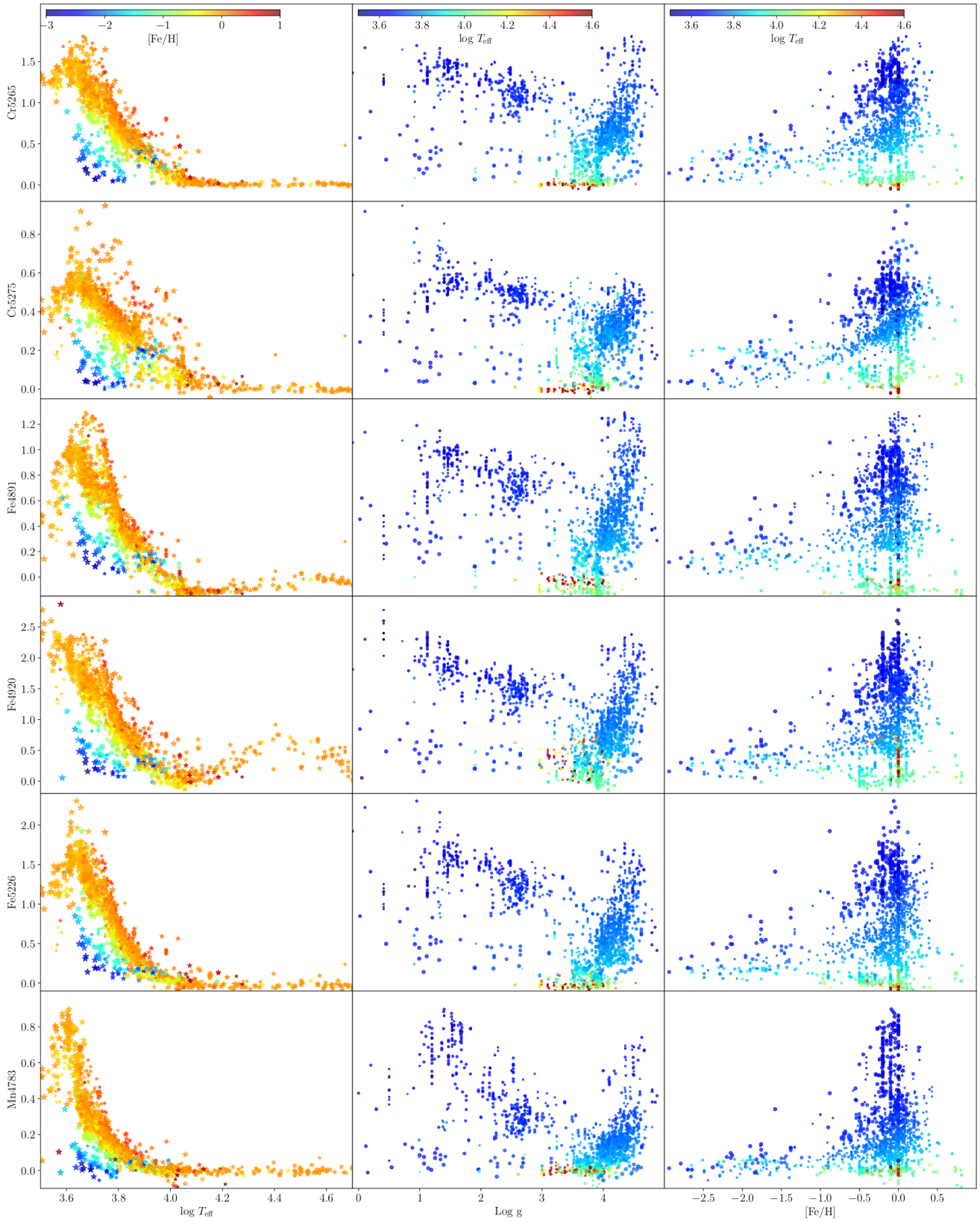

Figure C2. Same as in Figure C1 but for Cr5265, Cr5275, Fe4891, Fe4920, Fe5226 and Mn4783.

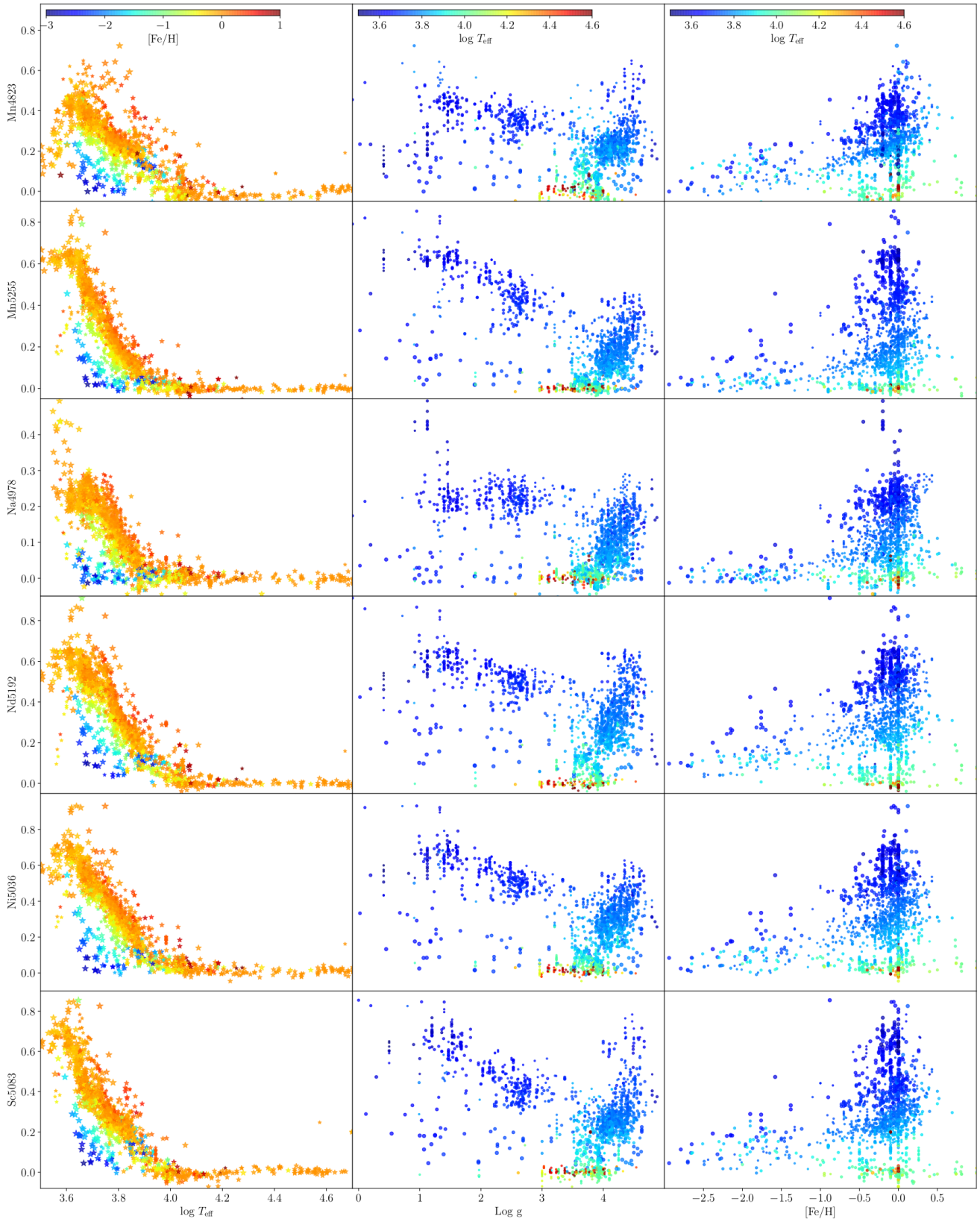

Figure C3. Same as in Figure C1 but for Mn4823, Mn5255, Na4978, Nd5192, Ni5036 and Sc5083.

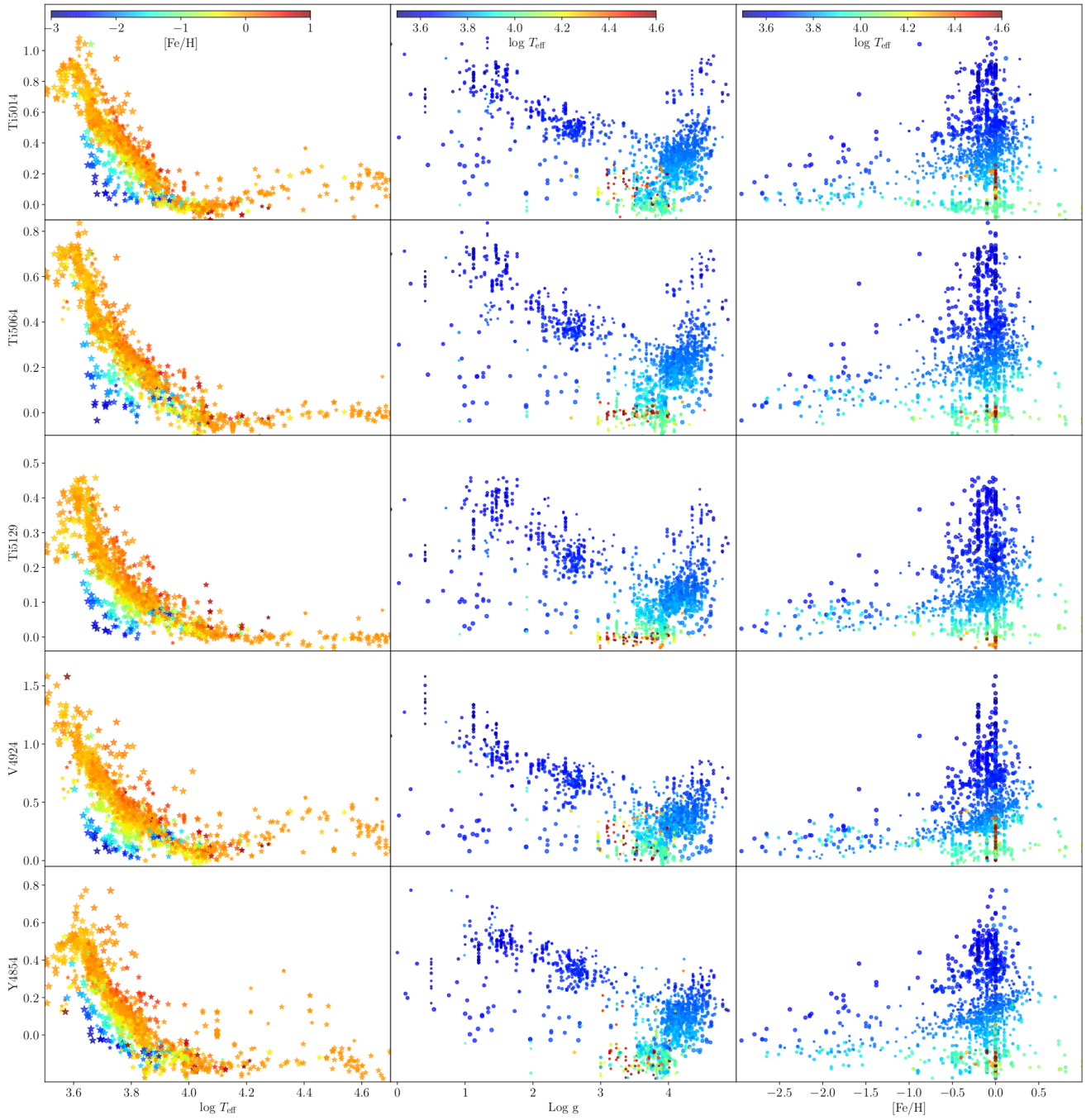

Figure C4. Same as in Figure C1 but for Ti5014, Ti5064, Ti5129, V4924 and Y4854.

APPENDIX E: COMPARISON MODELS WITH MILES AND PEGASE

We compare the line indices measured from the PEGASE and MILES SSPs.

This paper has been typeset from a TEX/LATEX file prepared by the author.

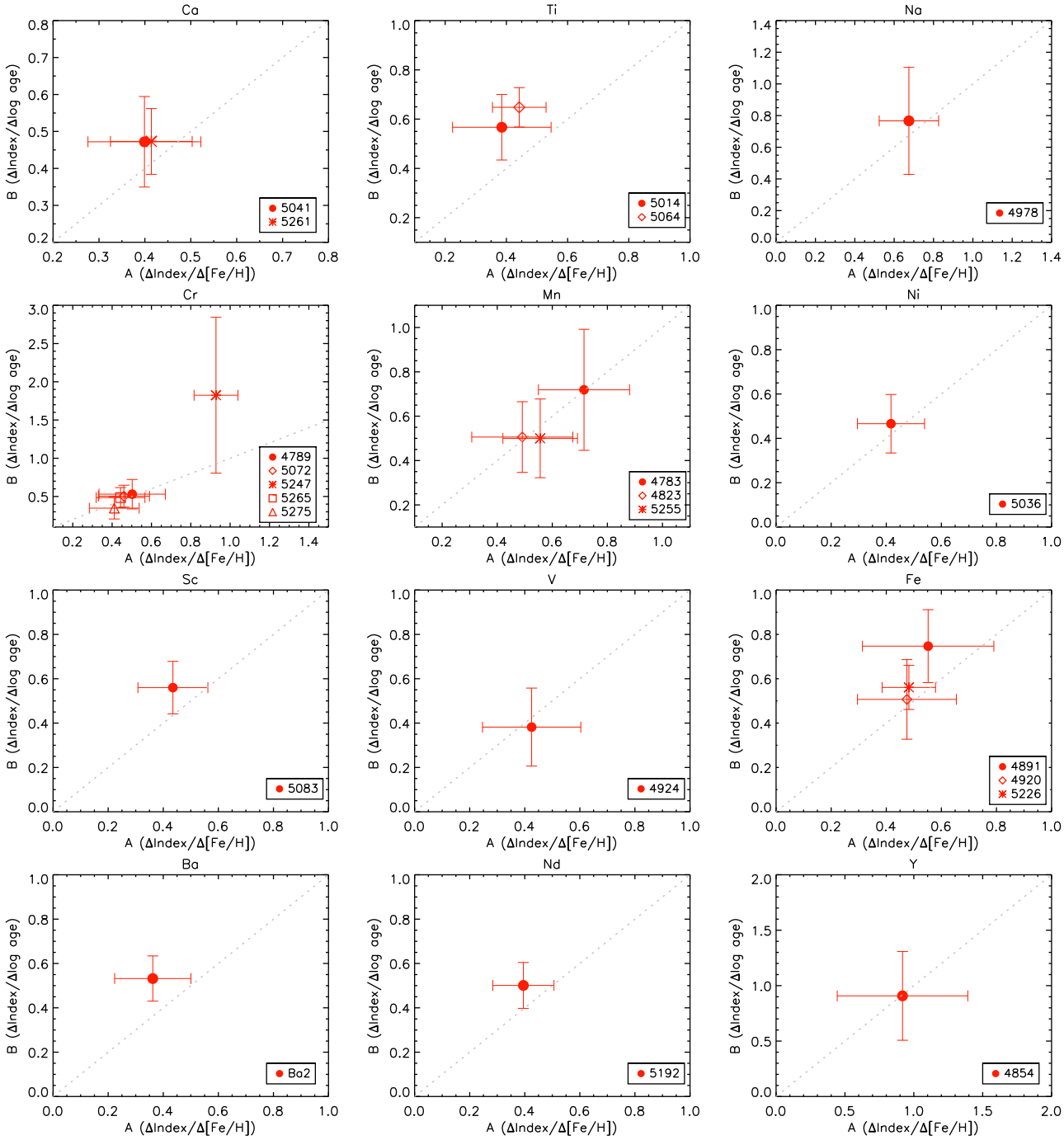

Figure D1. Comparison of age and metallicity dependence for Ca, Na, Y, Ba, Nd, Ti, Co, Cr, Mn, Ni, Sc, V and Fe elements. Data points near the X-axis are metallicity-indicators, while the ones near the Y-axis are age indicators.

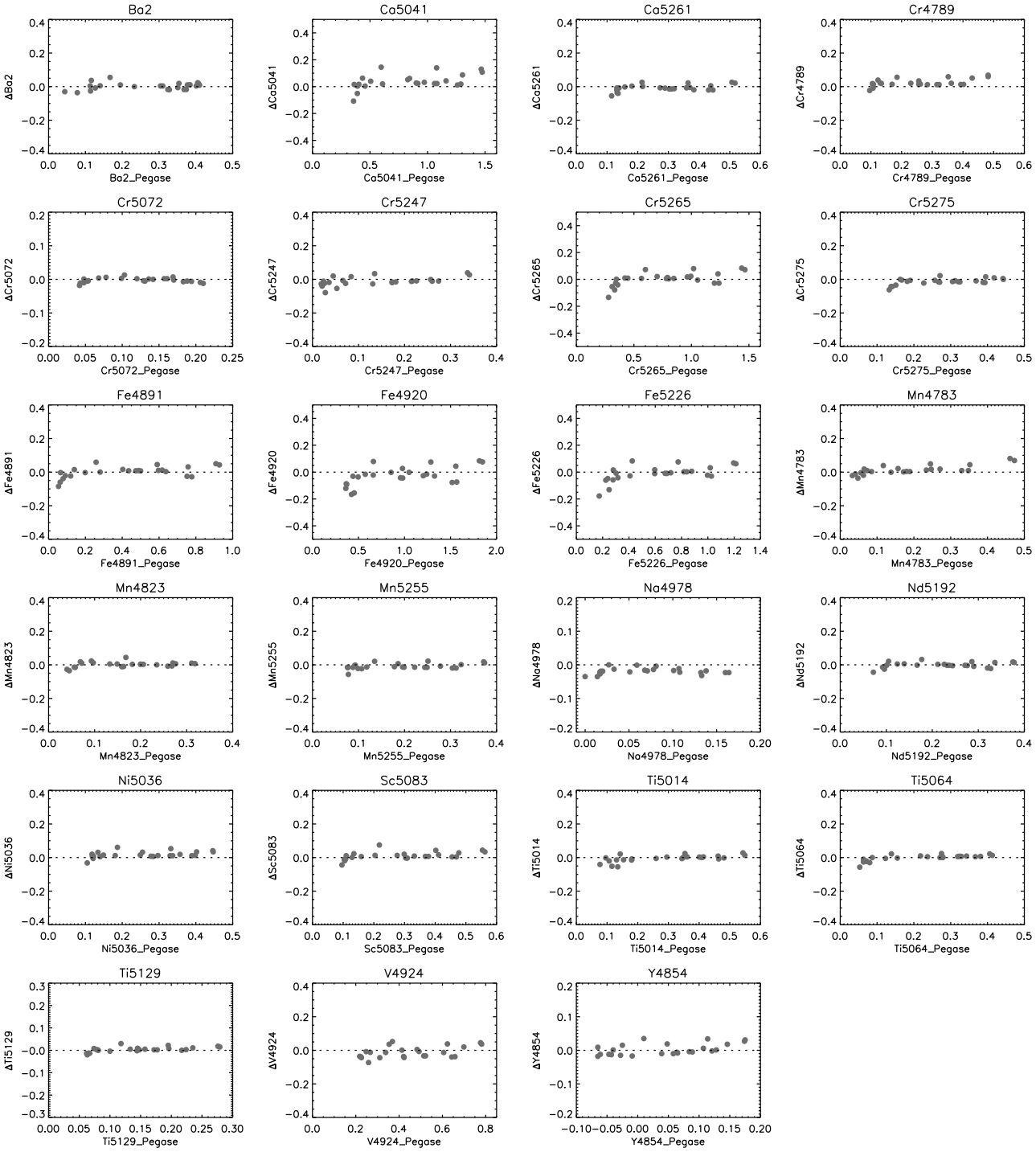

Figure E1. Our indices measured from MILES and PEGASE with 60km/s Here, $\Delta index = index_{\mathrm{PEGASE}}$ - $index_{\mathrm{MILES}}$

.